Published in Composites B, 295, 112153, 2025

DOI: https://doi.org/10.1016/j.compositesb.2025.112153

Does the Snow Queen Like Black? Nanocarbon and Biosilica-Reinforced THV-Based Anti-Icing Sponges

Emil Korczeniewski[1], Paweł Bryk[2], Ewa Olewnik – Kruszkowska[3], Piotr Kowalczyk[4], Agnieszka Z. Wilczewska[5], Karolina H. Markiewicz[5], Sławomir Boncel[6,7], Samer Al-Gharabli[8,9], Myroslav Sprynskyy[10], Michał Świdziński[11], Dariusz J. Smoliński[11], Kazunori Fujisawa[12], Takuya Hayashi[12,13], Przemysław Płóciennik[14], Joanna Kujawa[3,*] and Artur P. Terzyk[1,*]

1) Faculty of Chemistry, Physicochemistry of Carbon Materials Research Group, Nicolaus Copernicus University in Toruń, Gagarin Street 7, 87-100 Toruń, Poland,
2) Faculty of Chemistry, Institute of Chemical Sciences, Chair of Theoretical Chemistry, Maria Curie - Skłodowska University, Maria Curie-Sklodowska Square 5, 20 - 031 Lublin, Poland,
3) Faculty of Chemistry, Department of Physical Chemistry and Physical Chemistry of Polymers, Nicolaus Copernicus University in Toruń, Gagarin Street 7, 87-100 Toruń, Poland,
4) School of Mathematics, Statistics, Chemistry, and Physics, Murdoch University, WA, 6150, Australia,
5) Faculty of Chemistry, University of Bialystok, Konstanty Ciolkowski Street 1K, 15-245 Białystok, Poland,

6) Faculty of Chemistry, NanoCarbon Group, Department of Organic Chemistry, Bioorganic Chemistry and Biotechnology, Silesian University of Technology, Krzywoustego Street 4, 44-100 Gliwice, Poland,

7) Centre for Organic and Nanohybrid Electronics (CONE), Silesian University of Technology, Konarskiego 22B, 44-100 Gliwice, Poland

8) Pharmaceutical and Chemical Engineering Department, German Jordanian University, Amman 11180, Jordan,

9) College of Integrative Studies, Abdullah Al Salem University (AASU), Block 3, Khaldiya, Kuwait

10) Faculty of Chemistry, Department of Environmental Chemistry and Bioanalytics, Nicolaus Copernicus University in Toruń, Gagarin Street 7, 87-100 Toruń, Poland,

11) Department of Cellular and Molecular Biology, Nicolaus Copernicus University in Toruń, Lwowska Street 1, 87-100 Toruń, Poland, and Centre for Modern Interdisciplinary Technologies, Nicolaus Copernicus University in Toruń, Wileńska Street 4, 87-100 Toruń, Poland,

12) Research Initiative for Supra-Materials, Shinshu University, 4-17-1 Wakasato, Nagano, 380-8553, Japan,

13) Faculty of Engineering, Shinshu University, 4-17-1 Wakasato, Nagano, 380-8553, Japan,

14) Faculty of Physics, Astronomy, and Informatics, Department of Automation and Measurement Systems, Nicolaus Copernicus University in Toruń, Grudziądzka Street 5, 87-100 Toruń, Poland.

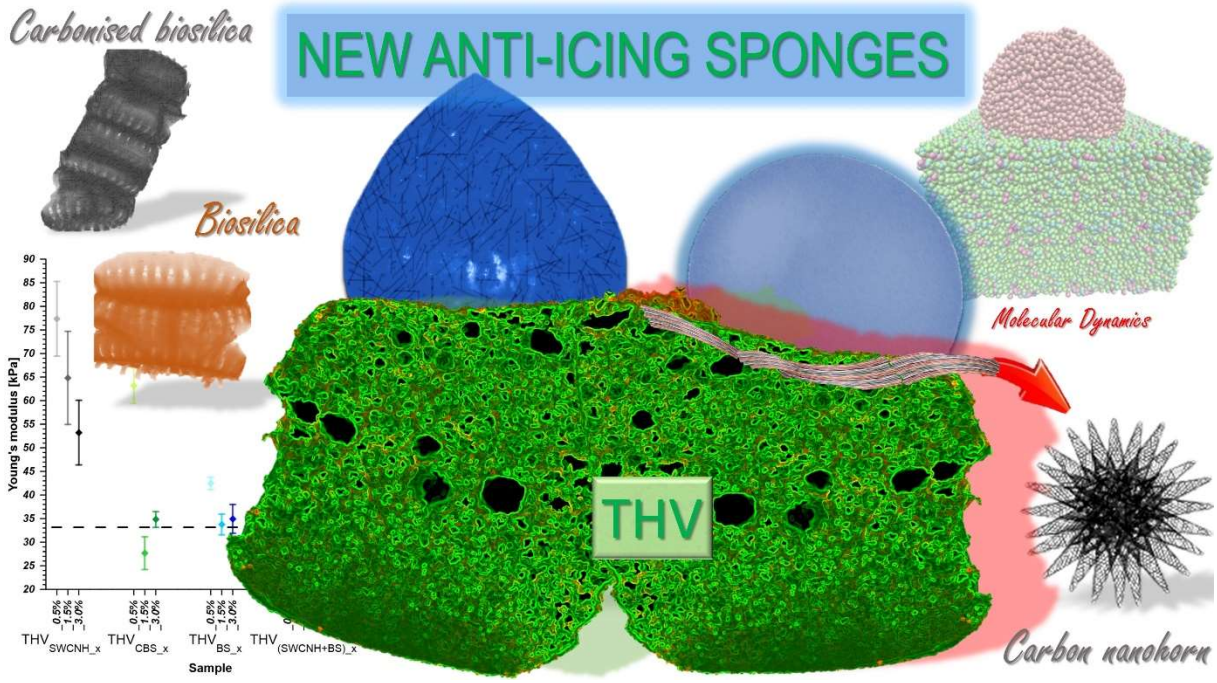

Abstract: New superhydrophobic, anti-icing tetrafluorethylene-hexafluorpropylene-vinylidenfluoride terpolymer (THV)-based materials: nonporous solids as well as porous sponges were created and deeply characterized using thermal analysis, spectroscopy, resistivity measurements, cyclic compression tests, and confocal microscopy. Single Walled Carbon Nanohorns (SWCNHs), biosilica (BS) as well as carbonized biosilica (CB) were applied as fillers. The "combined" origin of superhydrophobicity is explained based on experimental water contact angles (WCA) and molecular dynamics (MD) as well as Hansen Solubility Parameters (HSP) analysis. For all materials thermal resistance is improved after the addition of fillers, but among the studied samples only for the sample containing SWCNHs the application of electrothermal/Joule heating to reinforce anti-icing properties is possible. We propose a new forcefield for MD simulation of THV wetting. Moreover, MD results revealed that water freezing at the "flat" THV surface was moderately inhibited with respect to the bulk freezing and considerably inhibited with respect to the graphene surface. Introduction of SWCNHs to THV causes not only remarkable improvement of mechanical properties but also the improvement of anti-icing properties, especially to the stage of recalescence. The comparison of results for porous and nonporous materials led to new correlations describing freezing on the cold plate process, being a starting point for future studies on a new model describing the freezing mechanism. The most important conclusion of the complex study (around 100 samples altogether) is that the creation of mechanically resistant THV-SWCNHs-containing sponges is the most promising strategy in modern anti-icing science leading not only

to enhancement of the compression Young's modulus and the time to recalescence, but also to the drop of freezing temperature.

Keywords: THV, carbon nanohorns, biosilica, anti-icing, cold plate, Molecular Dynamics, Hansen Solubility Parameters.

1. Introduction

The studies on anti-icing carbon nanomaterials (CNMs)-reinforced surfaces, coatings [1] and especially sponges, are relatively rarely met in literature. Recent applications of CNMs-containing sponges are reported in fuel cells [2], piezoresistive sensors [3,4], magnetic field sensors and actuators [5], flexible piezoresistive devices [6], electromagnetic interference shielding materials [7–9], scaffolds for tissue engineering [10], liquid phase adsorbents [11–14], oil/water separation systems [15–20], mechanosensing devices [21,22], high-sensitive [23], pressure [24] and motion [25,26] sensors, supercapacitors [27], stretchable – negative Poisson's ratio capacitors and conductors [28], and antibacterial solids [29]. Among the most complex and demandinguses, Zhang et al. [30] reported reduced graphene oxide (rGO)-reinforced polyurethane and poly(vinyl chloride) sponges for application in multi-dimensional electronic mechanical sensors. The authors reported a high-sensitivity one-dimensional sponge applicable even for the detection of an impact caused by a hair. Other polymers and CNMs are also applied for the synthesis of sponges. Thus, Cheong et al. [31] applied for this purpose a polyimide and carbon black composite (synthesized using freeze-drying and heat treatment). The materials were characterized *via* porosity, density, and specific pore volume measurements. With the rise in carbon black content, the density of sponges and compressive stress increased, in contrast to porosity. Poly(vinyl alcohol) and formaldehyde were applied by Sun et al. [32] for the synthesis of GO-containing sponges with excellent mechanical resistance and high methylene blue adsorption. Melamine-formaldehyde foam was applied as a template for the catalytic growth of carbon nanotubes (CNTs) [33]. The creation of cracks and voids was analyzed by in-situ electron microscopy observation. Zhao et al. [34] showed that application of (pristine and boron-modified) CNT sponges to reinforce polydimethylsiloxane could lead to mechanically resistant composites, and Jiang et al. [35] pointed out that the preparation of low density sponges (density lower than 100 mg/cm^3) is still a challenge. Chen et al. [7] pointed out the critical influence of the drying process on the porous structure of sponges. Among the considered methods, due to its lowest cost, ambient pressure drying is the most common. This

method was applied in our previous study [36] as well as in the current study. However, to avoid its major disadvantage, *i.e.*, capillary forces driven collapse of pores [7], we introduced NaCl into the system. This salt can be easily removed by hot water.

In our previous report [36], the sponges composed of a terpolymer of tetrafluoroethylene, vinylidenefluoride, and hexafluoropropylene (THV) were studied. This relatively new polymer [37] was chosen due to its higher water contact angle (WCA measured in this work = 101.6±2.2°) compared to widely applied poly(vinylidene fluoride) (PVDF) (WCA = 95.6±1.5°) [36], hence it is more suitable for anti-icing strategy due to higher water repellency. Based on Hansen Solubility Parameters (HSP), we examined the influence of a solvent on sponge anti-icing properties. It was concluded that the most prospective properties were observed for the TVH sponge synthesized in the presence of an *N*,*N*-dimethylformamide (DMF) mixture with acetone (AC) (denoted previously as THV_{DMFAC}). This is why we applied such a mixture in this study. Since it is well known that CNMs can increase anti-icing properties [38,39], in the current report the THV sponge was combined with hydrophobic single-walled carbon nanohorns (SWCNHs) to improve icephobicity and mechanical properties of the material. Since hydrophilic diatoms are applied in anti-icing systems [40] as containers for anti-freezing substances, diatom biosilica (BS) was additionally applied in this study, as well as hydrophobic carbonized biosilica (CBS). Additionally, the mixture of hydrophilic (BS)-hydrophobic (SWCNHs) fillers was studied. Mechanical properties belong to the parameters that can be significantly influenced by fillers. For this reason, cyclic compression tests were carried out to determine such parameters as the maximum force at a deformation of 80% and changes in force during the relaxation process. Moreover, the obtained results allowed for the calculation of the energy required to achieve the given deformation, Young's modulus (YM), and compressive stress values.

Summing up, none of the tested nano/micro materials have been used in the THV matrix to create CNM-containing anti-icing sponges yet. Moreover, since it was concluded that surface roughness has a small influence on freezing time delay for hydrophobic surfaces [41] our next purpose is to check the validity of this conclusion. Combining the obtained results in this studyof freezing on a cold plate (more than 100 samples altogether) together with the thermogravimetric analyses, Hansen Solubility Parameters (HSP) calculations, Molecular Dynamics (MD) simulations, and mechanical properties allows us to propose new anti-icing, mechanically resistant sponges. Additionally, since carbon nanomaterials are applied in modern

anti-icing surfaces utilizing Joule – heating [42] the new sponges containing SWCNHs have been shown to be promising if the anti-icing properties can be reinforced by anisotropic Joule heating. Finally, our results shed new light on the mechanisms of freezing on a cold plate, revealing some new correlations that describe this process. The importance of freezing on the cold plate in everyday life, as well as recent developments in the study of its mechanism, were recently reviewed by Mengjie et al. [43] showing the importance of the research on the process mechanisms.

2. Experimental

2.1. SWCNHs

We applied SWCNHs from Carbonium, Selvazzano Dentro, Italy. After spraying on PVDF membrane, we observed the same water contact angle as for SWCNHs applied previously [44] (NEC, Tokyo, Japan). The TEM inspection showed that the diameters of SWCNHs are the same as those produced by the NEC company. Summing up, both materials (if one considers wetting properties and the diameters of dahlia flower nanoparticles) can be considered the same.

2.2. Diatom biosilica and pyrolyzed diatom biomass

The diatom biomass and diatom biosilica were obtained by the cultivation under laboratory conditions of the diatom species *Pseudostaurosira trainorii*. This diatom species was provided by the Culture Collection of Baltic Algae, Institute of Oceanography, University of Gdansk, Poland. Microalgae were cultured in 25 L photobioreactors containing the solution of artificial sea water (8 PSU) with Guillard's (F/2) growth medium and silicon at a concentration of 7 mg/L in the state of potassium metasilicate ($Na_2SiO_3 \cdot 5H_2O$), under air aeration, light regime 12 h light/12 h darkness, and at a constant temperature of 22 °C. The pH value of the culture solution was adjusted to 8.4. Diatom biomass was separated after the specified growth time (12 days) by decantation, washed five times with distilled water using centrifugation to remove dissolved salts, and dried at 60 °C. The dry weight production of diatom biomass was around 450 mg/L. The diatom biomass was pyrolyzed in a ceramic crucible placed into a quartz tube with heating under an argon flow of 100 °C/h in a programmable horizontal tube furnace PRW 75/LM (Czylok, Jastrzębie-Zdrój, Poland), maintaining at a temperature of 800 °C for 2 h.

Diatom biosilica (diatom exoskeletons) was isolated from dried diatom biomass using a 30% H_2O_2 solution to remove organic matter from diatom cells and 37% hydrochloric acid to remove calcium carbonates. The purified diatom biosilica was washed with distilled water using

centrifugation and dried in an oven at 120 °C. The physicochemical properties of the studied diatom biosilica as well as diatom biomass have already been given previously [45,46].

2.3. Preparation of THV "bulk" and "layered" sponges and reference "flat" THV

NaCl (Chempur, Piekary Śląskie) was ground twice by passing it through an EGK 200 W mill (Rommelsbacher ElektroHausgeräte GmbH, Dinkelsbühl, Germany) and then sieved on analytical sieves (sieve shaker LPzE-2e, Multiserw Morek, Marcyporęba, Poland) selecting a mixture of fractions 32-38 μm and 25-32 μm (1:2.7, m:m; DIN ISO 3310-1). Thirteen THV terpolymer solutions were prepared with the composition 9.6 g THV + 20 mL AC + 30 mL DMF. The above solutions were left for two days on a shaker ES-20 (Grant Instruments Ltd., Cambs, England) at 200 rpm and 25 °C, then placed on magnetic stirrers until homogeneous dissolution. After two days, 10 mL of each suspension of fillers (i.e., SWCNHs, biosilica, carbonized biosilica, and the mixture of biosilica and SWCNHs (1:3, m:m) were prepared in a mixture of acetone with DMF (2:3, v:v). The suspensions were sonicated with ultrasounds for 10 min, using Bandelin sonoplus GM mini20 (Bandelin Electronic GmbH & Co. KG, Berlin, Germany, sonotrode type MS 2.5), then washed with 20 mL of a mixture of AC with DMF (2:3, v:v). The total volume of the solvent mixture for 9.6 g of THV was therefore 80 mL for each sponge. After combining the fillers with the polymer solutions, the mixtures were left on magnetic stirrers. After another 4 days, 48 g of the combined fractions of ground NaCl were poured into each of the mixtures and, after 3 h, transferred from the magnetic stirrers to the shaker (250 rpm). The next day, all mixtures were placed in an ultrasonic bath for 2 h, then poured onto a Petri dish according to the following procedure: after opening the bottle, the contents were foamed using a whipper frother (5500 rpm, 3.5 min.), and approx. 50 mL of each mixture was poured out uniformly (keeping a constant pouring time of 2.5 min). They were left to air dry at room temperature for 6 days, subsequently placed in a dryer (40 °C) for 4 days, turned upside down after initial drying. Next, they were transferred into separate vessels with deionized water for 10 days to rinse off NaCl until the electrical conductance was as for pure water. The water was changed twice a day, once a day was heated to 60-70 °C for 4 h. The rinsed sponges were dried again at 40 °C for 6 days.

"Bulk" sponges: The sponge made from THV 221 AZ (Dyneon GmbH, 3M AdMD, Burgkirchen, Germany) and obtained in the mixture of DMF and AC assures the best multifunctional properties [36] and as such has been taken as the starting point for the research presented in the current work. Moreover, to the pristine polymeric dope, the carbon-based

additives were added. THV_{BS_X} is the same sponge but containing *x* percent mass of biosilica, THV_{CBS_X} contains carbonized biosilica, and $THV_{(SWCNH+BS)\_X}$ contains a mixture (3:1, m:m of SWCNHs and BS). In all samples, *x*=0.0 (it denotes pure THV), 0.5, 1.5, and 3.0% mass content of fillers. These samples are described as "bulk" (about 4-mm-thick, 15 mm in diameter). For these samples, we measured mechanical and thermal properties, SEM and HRTEM images (including cross-sections).

"Layered" sponges: Since the further analysis of obtained "bulk" sponges revealed nonhomogeneous (gravity-driven) distributions of CNMs and BS in sponges, we decided to prepare "layered" films for "bulk" sponges (only for analogous samples with index x=3.0%). "Layered" samples were prepared with a Leica VT 1200 S, Leica Biosystems, Deer Park, IL, US vibratome. Due to its precise cutting, sections with a thickness of 500 micrometers on the Z-axis were prepared through the entire thickness of the sample. Two cutting methods were used, namely cutting from the top and the bottom, respectively. Fig. S1 shows applied notations for obtained in this way "layered" samples. Resistivity, anti-freezing properties, confocal, and SEM microscopy results were collected for "layered" sponges. For the notation given above, the number and the origin of a layer were added, thus for example: $THV_{SWCNH\_3.0\%\_2\_TOP}$ denotes the second (layer number *i*=2) "layered" sponge, cut from the top (TOP), and containing 3.0% wt. of SWCNHs.

"Flat" samples: The "flat" THV sample as well as the samples containing nano/micromaterials were prepared by melting (450 °C/h then constantly 190 °C held for 30 min) the polymer agglomerate between glass plates separated by the distance 0.5 mm and pressed by the weight on a thermostated digital hot plate (HP30A-2, Torrey Pines Scientific, Carlsbad, CA, US). "Flat" samples containing nano/micromaterials were cast by melting already produced sponges to ensure the most homogeneous dispersion of fillers in the polymer matrices. They were subjected to 3 weeks of degassing from air from their pores at a constant temperature of 190 °C. The samples were freely separated from the glass by the forces of surface tension under water. For "flat" samples, resistivity and anti-freezing properties were determined. The samples were denoted with subscript "F".

2.4. Sample analysis

2.4.1. Thermal Analysis

Thermal analysis was performed for the "bulk" sponges using a TGA/DSC 1 STARe System, Mettler-Toledo AG, Schwarzenbach, Switzerland . Measurements were performed in an argon or synthetic air atmosphere with a flow rate of 20 mL min^{-1}. Samples (2-3 mg) were analyzed

in an aluminum oxide crucible in the temperature range from 50 to 900 °C with a heating rate of 10 °C min^{-1}. An empty crucible was used as a reference. Calorimetric analysis was performed in an air atmosphere. The samples were analyzed in sealed aluminum crucibles in the temperature range from −100 to 300 °C with a heating rate of 10 °C min^{-1}. An empty crucible was used as a reference.

2.4.2. Optical and confocal microscopy, electrical conductivity

The morphology of "bulk" samples was studied using an HR-5000E (Hirox Europe, Limonest, France) 3D digital microscope. Scanning the entire surface of the sample along the Z-axis at high resolution was performed. The multiscan option was utilized to compile consecutive Z-axis images. During the imaging of the samples using a Leica SP8 confocal microscope (Leica Microsystems, Heidelberg, Germany), two phenomena were observed: fluorescence emission in the violet-blue range of 412-491 nm (marked in images by red color) and the emission of reflected light at the same excitation wavelength (marked in images by green color). In both cases, a 405 nm diode laser (50 mW) was used for excitation. The fluorescence was recorded using a photomultiplier tube (PMT) detector (Hamamatsu R 9624). As the fluorescence quantum efficiency was low, the laser power used for fluorescence excitation was as high as 30%. Tests showed that the material burned at the higher power of the laser; thus, 30% was established as the upper limit for the laser power in this detection. Multiple-repetition recording was employed, and an averaging function was applied to reduce high noise at a high gain of 751. The reflected light (Transmission Detection Line) from the material was detected at a low laser power of 0.10%, with the photomultiplier gain set to 451.

To check the possible application of electrothermal/Joule heating to enforce anti-icing properties, the measurements of electrical conductivity were recorded for "layered" and "flat" samples using a 4200-SCS Semiconductor Characterization System (Keithley Instruments, Inc., Cleveland, OH, US). Resistivity measurements were performed at an inter-electrode edge distance of 1 mm using the following contacts: brass flat disks (9.3 mm and 4.2 mm diameter) and gold flat disks (99.99% purity, 4.8 mm and 4.8 mm diameter). The measurement was repeated at least 10 times for each sample.

2.4.3 SEM and TEM imaging

SEM images (Quanta 3D FEG FEI Company, Hilsboro, OR, US) were collected for cross sections and top view for "bulk" samples. In order to prepare samples for transmission electron microscope (TEM), bulk sponges were crushed into powder using the cryo-milling technique. Cryo-milling was performed with a 6775 Freezer/Mill (SPEX SamplePrep LLC, Metuchen, NJ, US). With this instrument, the bulk sample was cooled down to liquid nitrogen temperature and then milled by a magnetically driven metal impactor at a rate of 10 cycles per second. The obtained powder sample was dispersed into ethanol solution, and then a drop of the dispersion was applied onto a TEM grid. TEM observation was conducted using a JEM-2100F (JEOL Ltd., Akishima, Japan) equipped with double spherical aberration correctors (CETCOR/CESCOR, CEOS) operated at 80 kV.

2.4.4 Contact angle and anti-icing properties

Water contact angle and anti-icing properties were determined using the system described in details previously – see [47] and ref. 48 therein, in the ambient air and with the following changed conditions and parameters. The samples were adhered to the surface of the cooling stage using thermally conductive double-sided copper SEM tape (Micro to Nano BV, Haarlem, Netherlands) to eliminate any thermal gap. The temperature of the droplet sitting onto the substrate was measured during the freezing process using the CTlaser LT, model OPTCTLLTCF2 (-50-975 °C/8-14 μm/ 75:1/ 120 ms/ 1.9 mm@150 mm) pyrometer (Optris GmbH, Berlin, Germany). Before each measurement, the water temperature in the thermostat was stabilized to a value equal to the ambient temperature (20±1 °C; ambient relative humidity equaled to 36-47%). After dispensing a 6 μL drop of deionized water (resistivity equaled 15 MΩ cm), the water thermostat and the Peltier power supply were switched on simultaneously. The water droplet temperature and the profile image of a water droplet sitting on the sample surface were recorded. The reproducibility of temperature drop profiles on the surface of the copper strips beneath the sponges is very high (see. Fig. S2).

2.4.5 Mechanical properties

Cylindrical composite samples and control sponges with a diameter of 19.0±0.2 mm and a height of 4.0±0.5 mm were subjected to uniaxial compression tests. All measurements were performed using the EZ-Test-SX 100N testing machine (Shimadzu Corp., Kioto, Japan). The obtained sponges were introduced between the pressing plates and pressed 20 times with the cross-head speed set at 10 mm/min to a compressive deformation of 80%. In every cycle, the materials, after squeezing, remained under constant load for 30 s. In the next stage of the

compression process, the probe returned to zero deformation with the same speed and remained in this position for 30 seconds.

2.4.6 Profilometry

Profilometric analyses were done using the optical profilometer Sneox (Sensofar Tech S.L. 2022, Barcelona-Terrassa, Spain). A 10×-magnification lens was used, Nikon Plan Fluor Epi class, lighting: monochrome, white, and green depending on the sample. SensoVIEW 1.9.2 software was used for image analysis. For calculating Ra, a standard cut-off (λ_S) was used at 8.00 µm, cut-off (λ_C) was used at 0.08 mm, according to ISO 4287. A free profile in the form of a straight diagonal line was averaged by extending it over the entire image, collected from an area of 1311.54 µm × 1744.85 µm, thresholded 0.10% from both ends.

2.5. Hansen solubility parameters

HSPs were implemented to determine the affinity between the sponges and water or ice to assess the anti-icing properties. Moreover, these tools enable to analyze the affinity between the THV material and carbon-based filler itself. During the calculation, the distance in the Hansen's sphere (R_a) and Relative Energy Difference (RED) were determined. The detailed explanation of the mentioned parameters is presented in our previous work [36].

2.6. Molecular Dynamics Simulation

Since in this study THV is simulated for the first time, the procedure of force field creation needs a detailed description. We model THV (with determined previously [36] mole fractions of 46.2% TFE, 41.9% VDF, and 11.9% HFF) as a random terpolymer composed of three different beads. The total number of segments was 33 and we used 15 segments of TFE (-CF_2-CF_2-), 14 segments of VDF (-CH_2-CF_2-), and 4 segments of HFF (-CF_2-$CFCF_3$-). This structure leads to the mole fractions of 46%, 42%, and 12% for TFE, VDF, and HFF, respectively [36]. The polymer was terminated with fluorine atoms at both ends. In modeling the THV chains, we used the united-atom GROMOS 54A7 ATB force field [48,49]. The main difference between the all-atom and the united-atom versions of the aforementioned force-field is that the latter does not treat the hydrogen atoms of the VDF segments explicitly. The reasoning behind this selection is that, in our approach, the water molecules are represented using the one-site monoatomic water (mW) model [50], hence the united-atom version seemed more appropriate. All molecular dynamics simulations were carried out using the LAMMPS simulation package [51]. The polymer surface was generated using the procedures outlined in [52]. The details of

system preparation and simulation are given in Supporting Information. WCA values were determined using the procedure described in our previous papers [52,53]. Freezing of water droplets was simulated using the setup identical to that used above. 6000 mW water molecules were placed on top of the THV surface. Next, MD simulations were performed in an NVT ensemble with 3 Nose-Hoover chains with time-step Δt of 5 fs and a relaxation time of 500Δt. A set of simulations began at the temperature –10 °C, then the temperature was gradually decreased with the colling rate 1 °C /ns until the final temperature was reached. The procedure of creation of THV rough surfaces was similar to applied previously [52] and is provided in Supporting Information together with other MD simulation details.

3. Results and discussion

3.1. Thermal Analysis

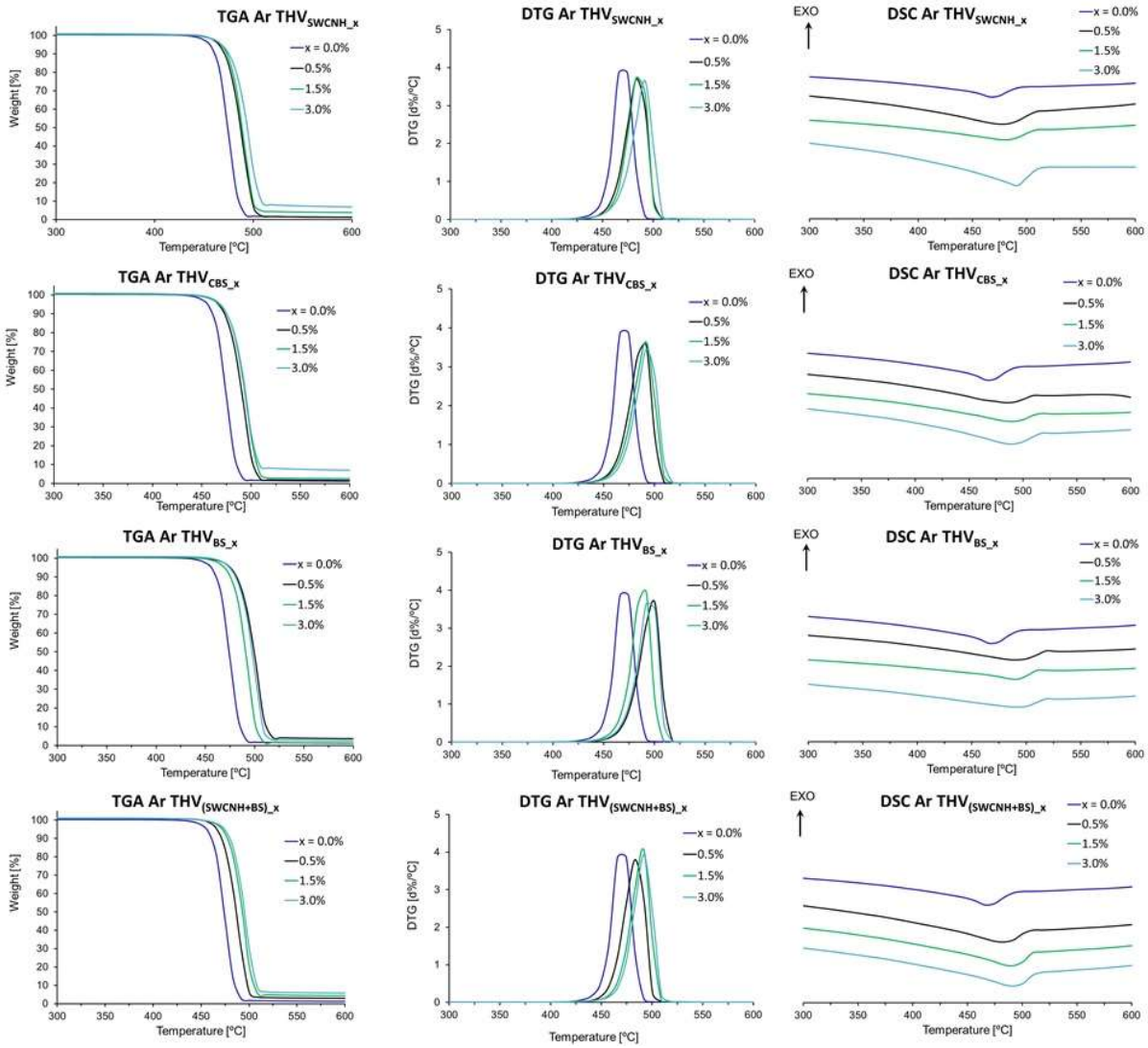

Figure 1. TGA, DTG, and DSC curves of studied materials obtained under argon atmosphere.

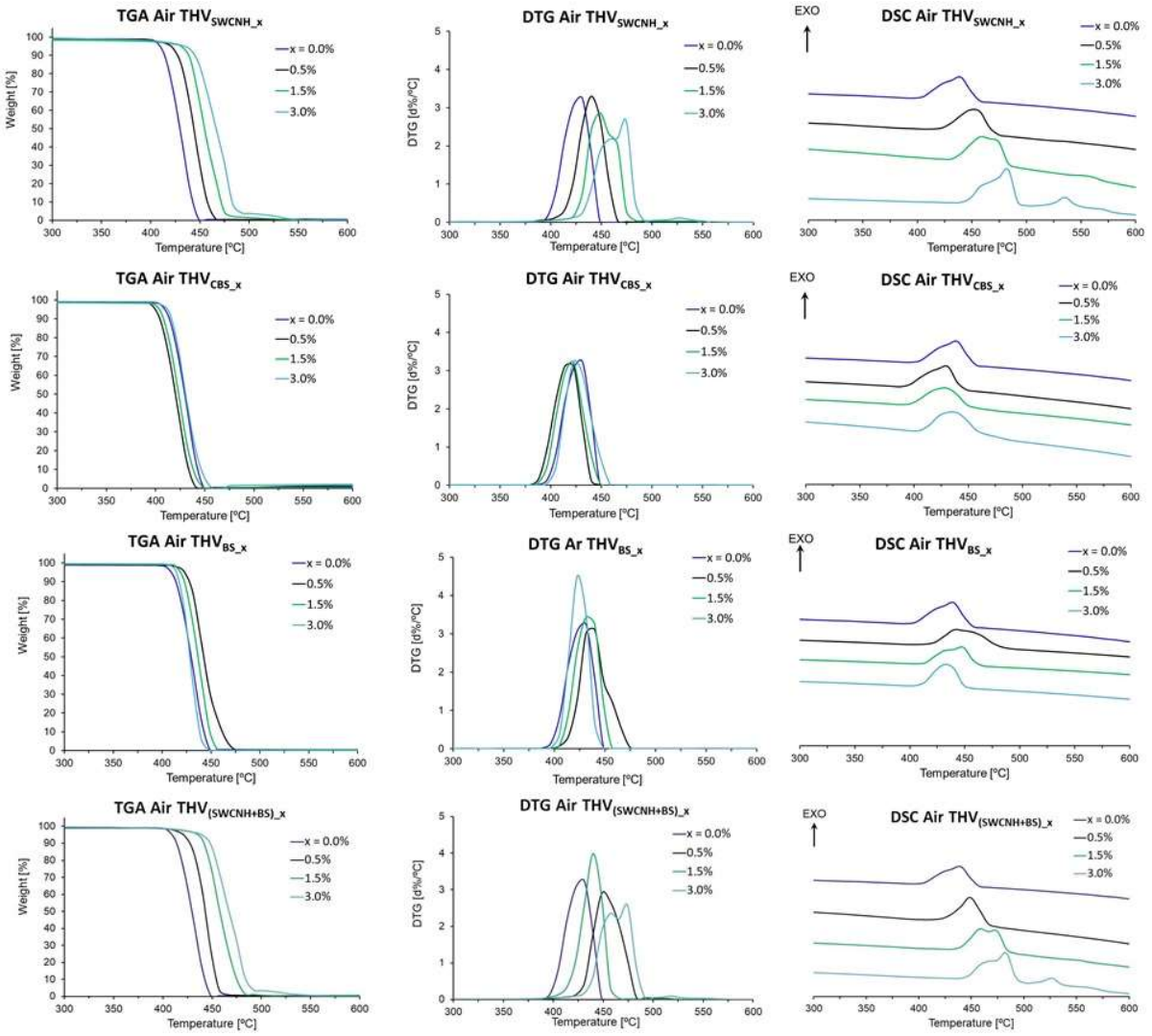

Figure 2. TGA, DTG, and DSC curves of studied materials obtained under air atmosphere.

The thermal properties of the materials were evaluated by thermogravimetric analysis (TGA) and differential scanning calorimetry (DSC) (Figs. 1, 2and Fig. S3). Simultaneous TGA/DSC analysis was performed in the air and argon atmosphere. The temperatures of the maximal weight loss (T_{max}) in air and argon are presented in Table S1. The pristine THV degrades quantitatively in one step between 425 and 500 °C in Ar and 375 and 450 °C in air. The modified materials also show a one-step degradation except for the two samples containing the highest amount of SWCNHs and BS, $THV_{SWCNH\_3.0\%}$ and $THV_{(SWCNH+BS)\_3.0\%}$, respectively. In the DTG curves performed in air, two maxima of the degradation rates are observed for these two samples. Primarily, the thermal stability of all modified samples is improved. Temperature ranges of degradation are shifted to higher values (425-520 °C in Ar and 370-500 °C in air). In general, the higher the content of an additive, the higher the degradation temperature. A

comparison of results obtained in air and Ar shows the influence of oxygen on the material decomposition process; in Ar, degradation is exothermic, and in air, it is endothermic. In the air, all samples are decomposed quantitatively, whereas, in argon, small residues related to the presence of additives, which do not decompose in the applied temperature range, can be observed.

DSC analysis was performed in the air. DSC curves (Fig. S3, Tab. S1) show the melting of the materials in a relatively broad temperature range of 75-150 °C. Only minor changes in the melting behavior of pristine and modified materials can be observed as expected. We also recorded small amount of residuals (including also NaCl) in studied samples (a peak around 800 °C), and the average amount of residuals is not larger than 0.6%.

3.2. Optical and confocal microscopy, resistivity

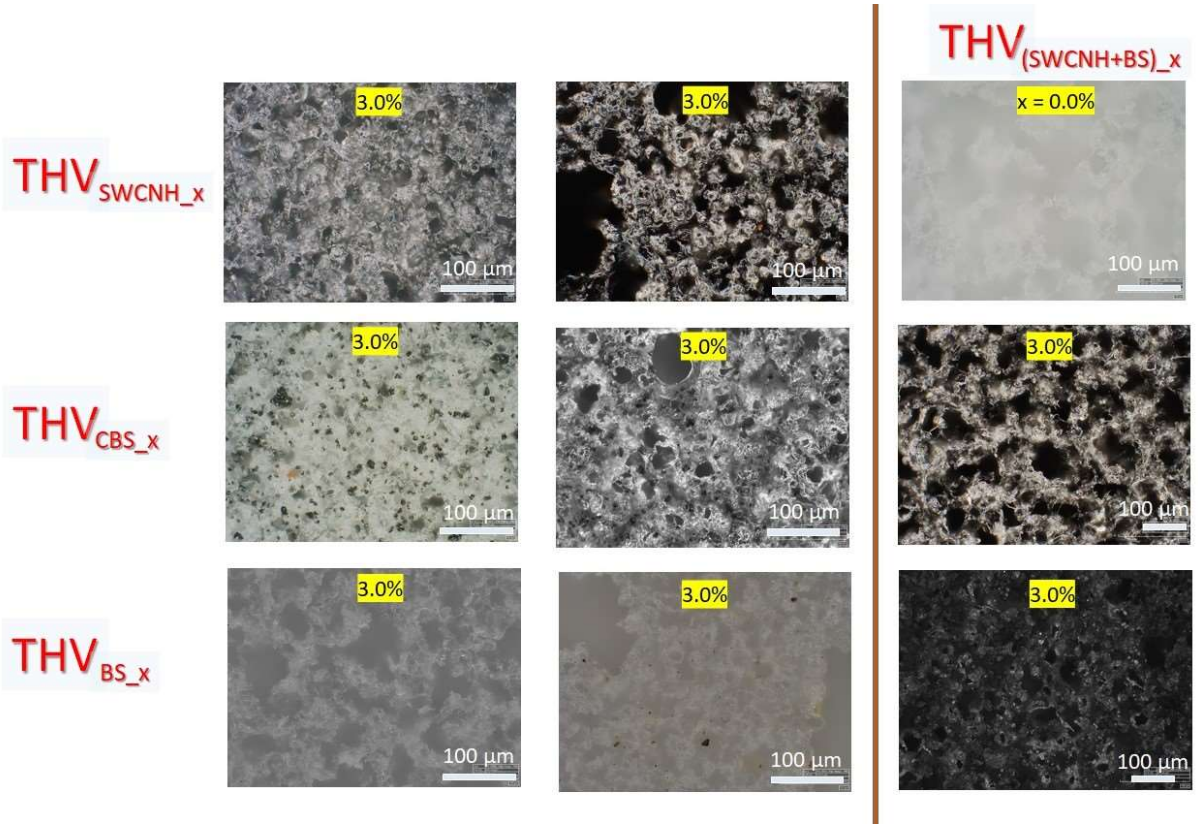

Figure 3. The results of optical microscopy for the initial polymer and for chosen "layered" samples.. The photos show the samples in the following order: $THV_{SWCNH\_3.0\%\_1\_TOP}$,

$THV_{SWCNH\_3.0\%\_1\_BOTTOM}$, $THV_{CBS\_3.0\%\_1\_TOP}$, $THV_{CBS\_3.0\%\_1\_BOTTOM}$, $THV_{BS\_3.0\%\_1\_TOP}$, $THV_{BS\_3.0\%\_1\_BOTTOM}$, initial THV, $THV_{(SWCNH+BS)\_3.0\%\_1\_TOP}$, $THV_{(SWCNH+BS)\_3.0\%\_1\_BOTTOM}$.

From the results collected in Fig. 3, one can see the formation of agglomerates of nanomaterials in polymer matrix. This process is the least visible for $THV_{BS\_3.0\%}$ sample since it is white.

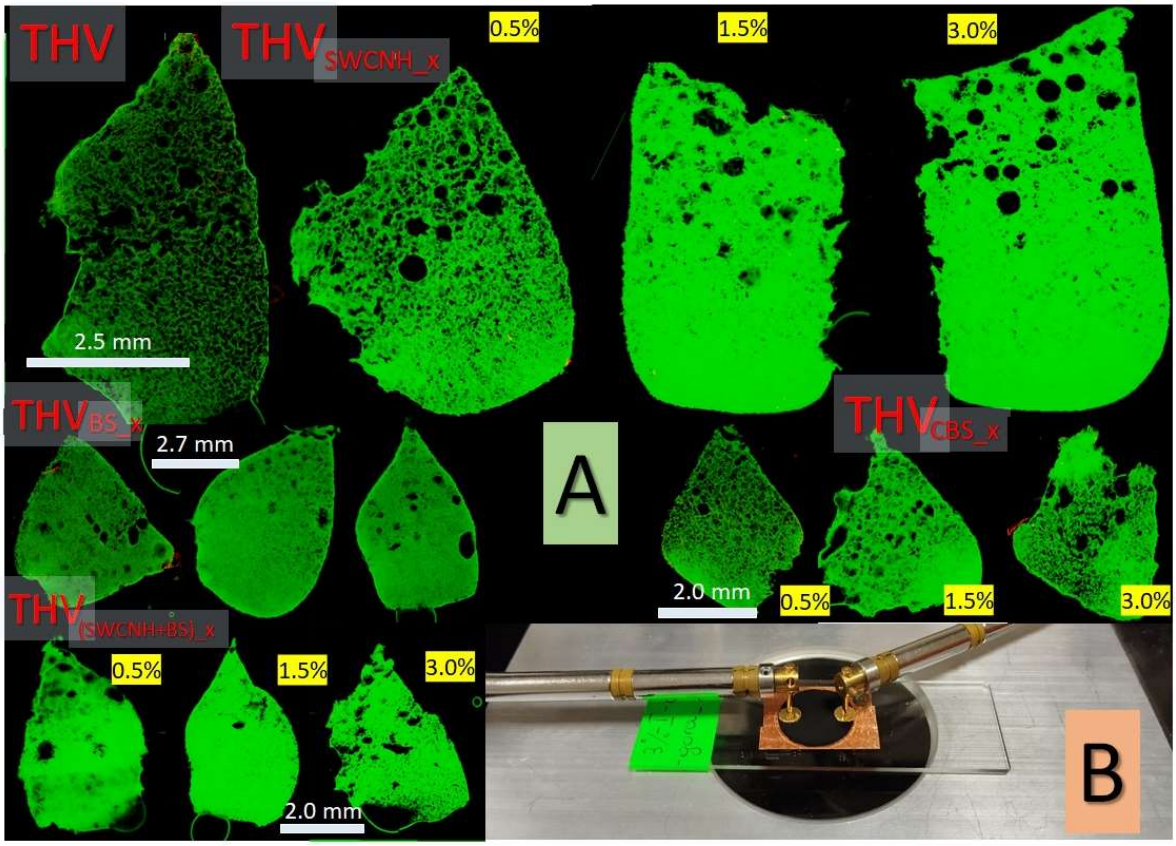

Figure 4. Confocal microscopy images of cross-sections (A) and the equipment for measurement of the electrical resistivity of studied samples (B).

Confocal microscopy images of cross-sections (Fig. 4) reveal a nonhomogeneous distribution of nano/micro agglomerates, however, the presence of pores may misperceive. It can be seen, for all samples containing nano/micro materials that the number of pores decreases in comparison to pure THV sponge. Also, nonhomogeneous distributions of large pores in samples are observed with smaller amounts at the bottom of the samples. However, the resistivity results measures using the equipment shown in Fig. 6B show nonzero values only for SWCNH sprayed and immersed in polymer and for $THV_{SWCNH\_3.0\%}$ (Fig. 5). Thus, among studied sponges, only for this one the application of electrothermal/Joule heating to enforce anti-icing properties is possible. This is the reason why the sponges containing 3% of nano/micro materials were chosen for the study of anti-icing properties.

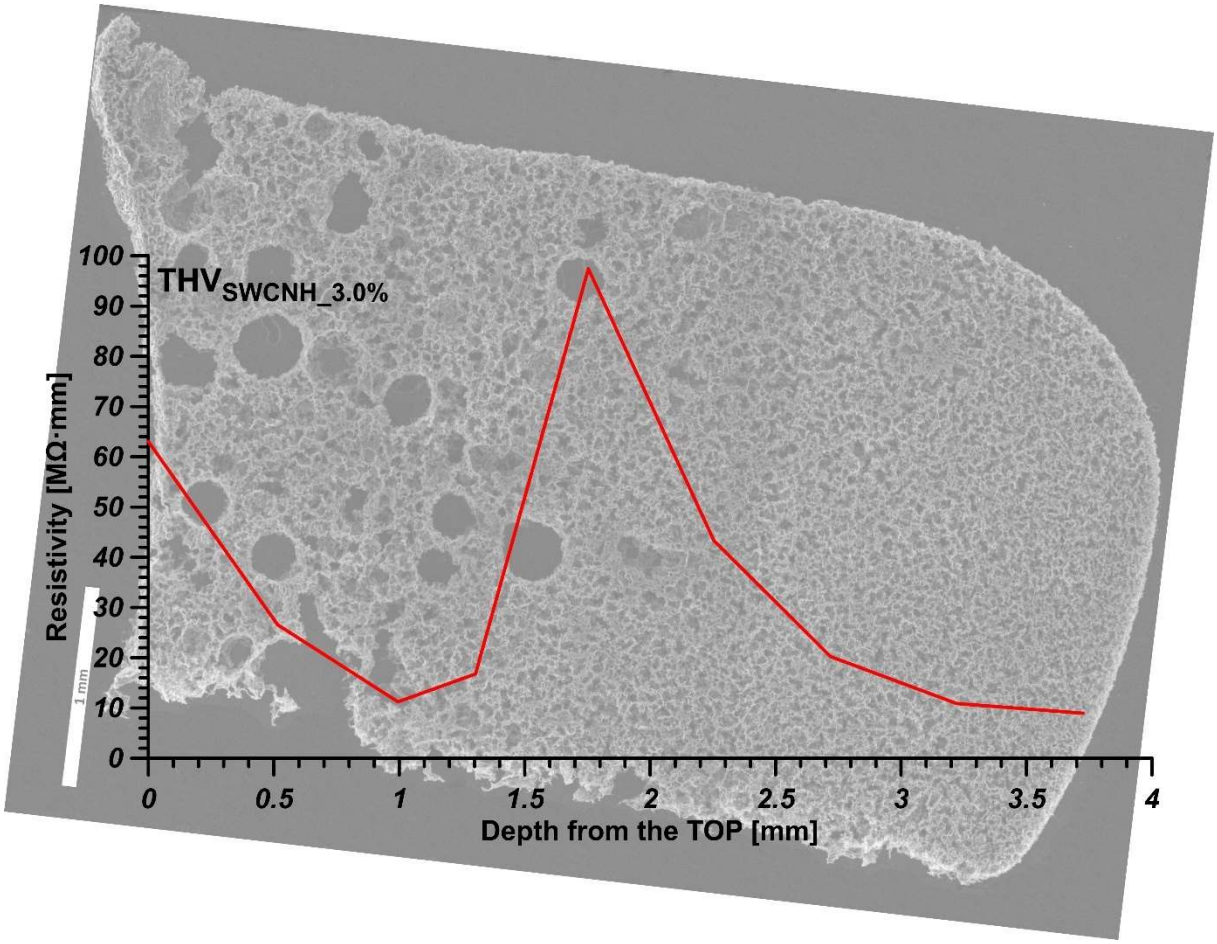

Figure 5. Resistivity of $THV_{SWCNH\_3.0\%}$ plotted as a function of distance from the TOP of the tested sample with the SEM image of their cross-sections shown as a background.

It is seen (Fig. 5) that the values of resistivities, due to the heterogeneous distribution of SWCNHs in the sample depend on the depth from the outer surface of the sponge. At the bottom, it decreases, and this is with excellent agreement with the confocal microscopy and SEM results (Figs. 4 and 6).

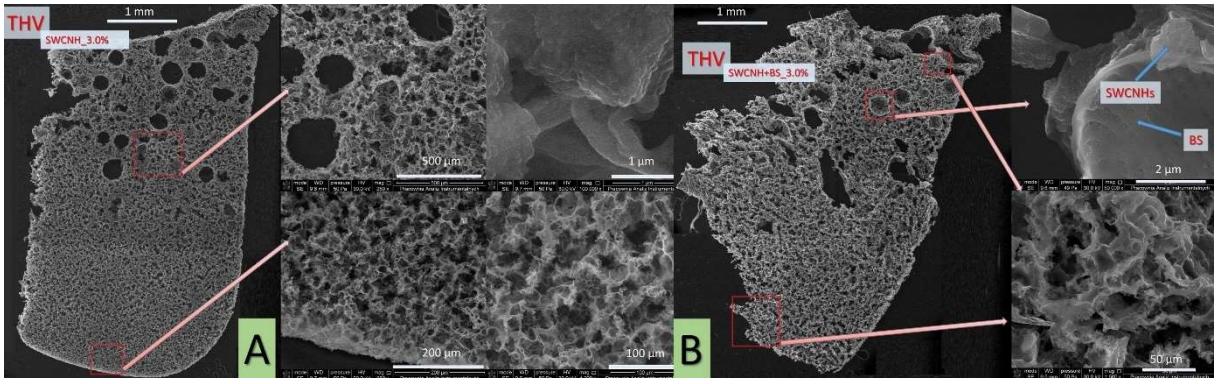

Figure 6. SEM images of the cross-sections (see Fig. 6) of $THV_{SWCNH\_3.0\%}$ (A) and $THV_{(SWCNH+BS)\_3.0\%}$ (B).

Fig. 6 collects SEM results for the samples $THV_{SWCNH\_3.0\%}$ (A), and $THV_{(SWCNH+BS)\_3.0\%}$ (B). One can observe the creation of nanocables from SWCNHs immersed in THV. In contrast, for $THV_{(SWCNH+BS)\_3.0\%}$, the creation of SWCNH aggregates located in the vicinity of THV occurs. The out-of-range high resistivity for this sample can be caused by the smaller amount of SWCNHs. It is well known [54] that the power of the Joule heating system, *i.e.*, the energy converted in time units into heat, is proportional to resistivity. It means that the $THV_{SWCNH\_3.0\%}$ system is a good material for Joule heating on a width no larger than ca. 1 mm. This distance can be increased by increasing the percentage of nanomaterial in the polymer matrix. Our research shows the lower limit value of this content. This is an excellent property, especially if anisotropic Joule heating is necessary, for example, only in a given direction or a given plane (like a skin on a polymer cast) of an anti-freezing layer. By initially selecting the conditions of the polymer mass aeration process and the shape of the vessel for its casting, it is possible to obtain directional areas of greater porosity (fewer connections between charge-carrying particles) and areas with filler density allowing for Joule heating. Due to the applied polymer and sample flexibility, it is possible the applicability of the obtained sponges in flexible, anti-freeze clothing and wearable applications [55]. In summary, as the optimal resistivity of a given material greatly depends on the specific balance between heat generation, electrical efficiency, and operational/ thermal stability in air, for the herein designed and elaborated materials one might expect a convenient, tunable scalability toward Joule heating-driven deicing.

3.3. SEM and TEM images

Interestingly, the detailed analysis of SEM images does not reveal a large amount of nano/micromaterials on surfaces, except $THV_{SWCNH\_3.0\%}$ (Fig. 7 – blue arrow). The results of optical microscopy indicate that a layer of THV does not fully cover nano/micromaterials in most cases (Figs. 8-10). This layer is relatively thin, thus we observe agglomerates on optical images. Generally, the analysis of the top, bottom, and cross-sections of the "bulk" sponges reveals differences in the morphology of studied materials (in the manuscript we present only the top (surface) layers (i=1 Fig. S1), the remaining images are presented in Figs. S4-S11).

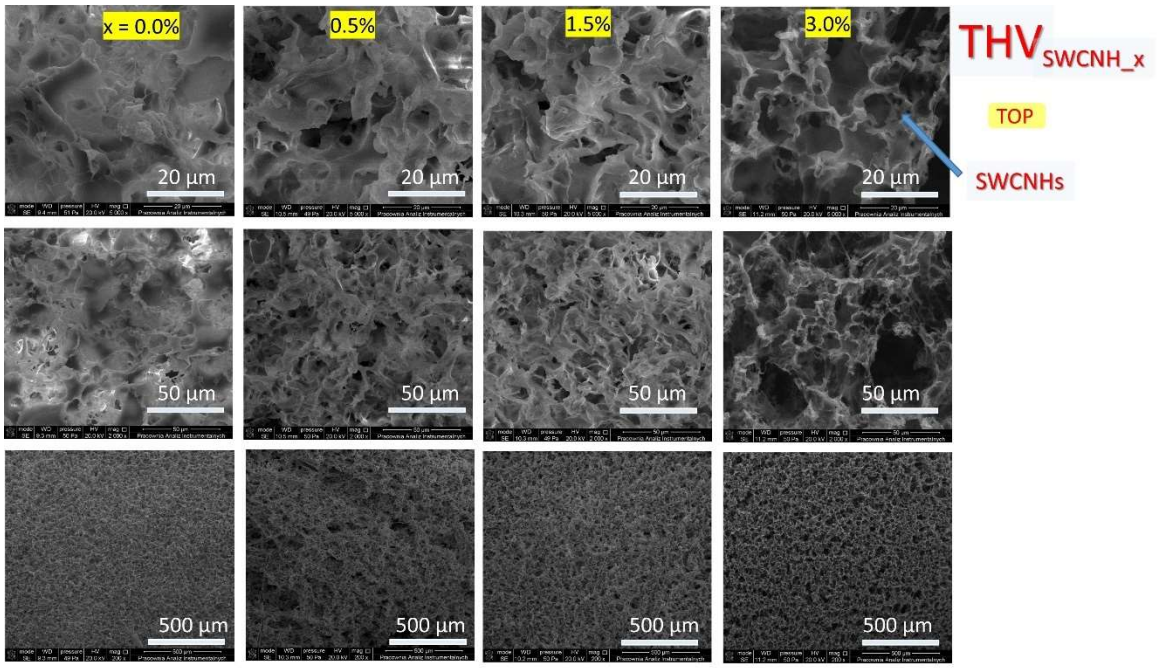

Figure 7. SEM images for the top layers (i=1) of $THV_{SWCNH\_x\_1\_TOP}$ (blue arrow shows SWCNH aggregates).

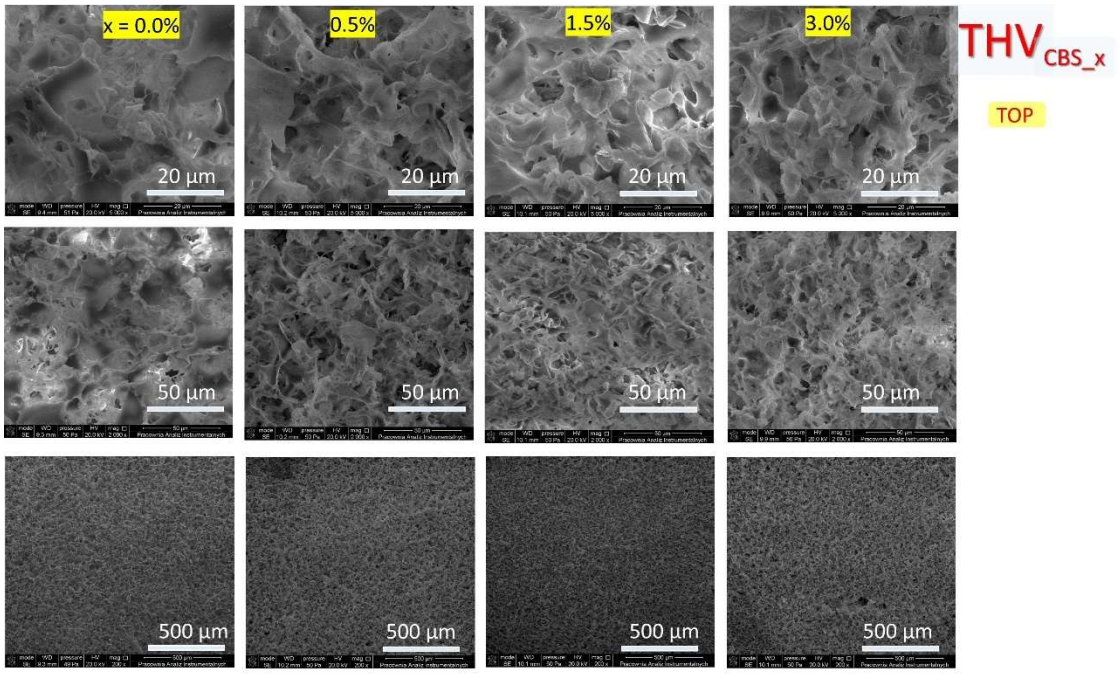

Figure 8. SEM images for the top layers of $THV_{CBS\_x\_1\_TOP}$.

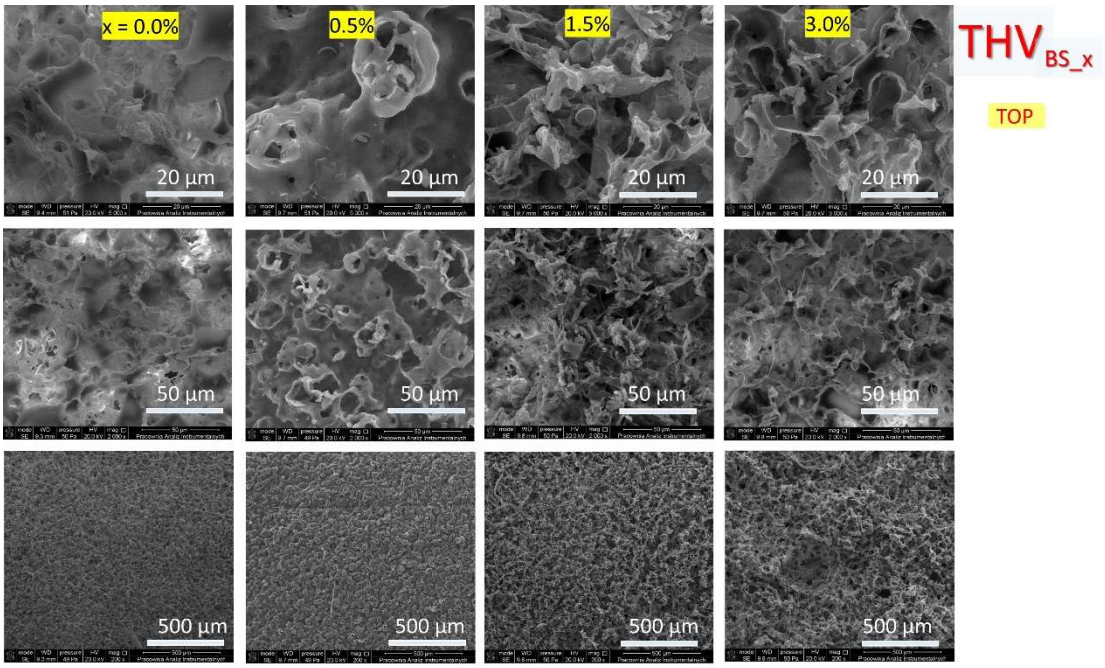

Figure 9. SEM images for the top layers of $THV_{BS\_x\_1\_TOP}$.

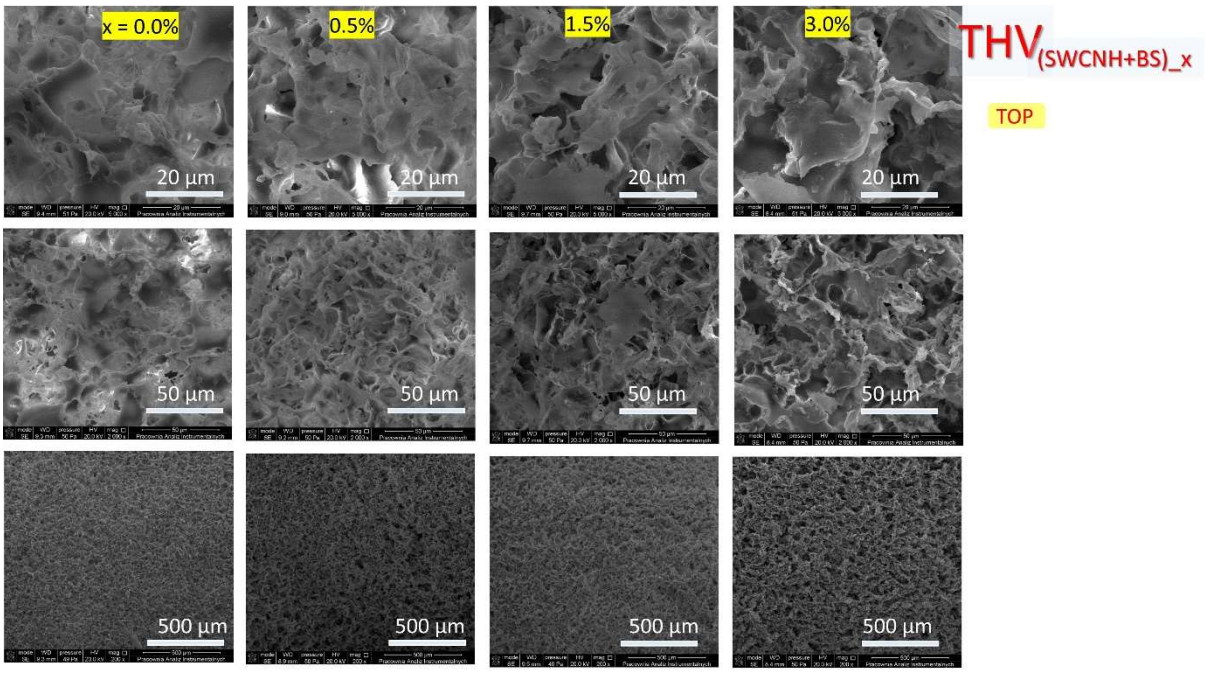

Figure 10. SEM images for the top layers of $THV_{(SWCNH+CBS)\_x\_1\_TOP}$.

Fig. 11 presents the TEM images for the initial nano/micro materials. As one can observe, there are remarkable differences in the diameters of nano/micro objects. SWCNHs are in the form of bundles with diameters of ca. 60 nm, while BS and CBS have sizes of several micrometers.

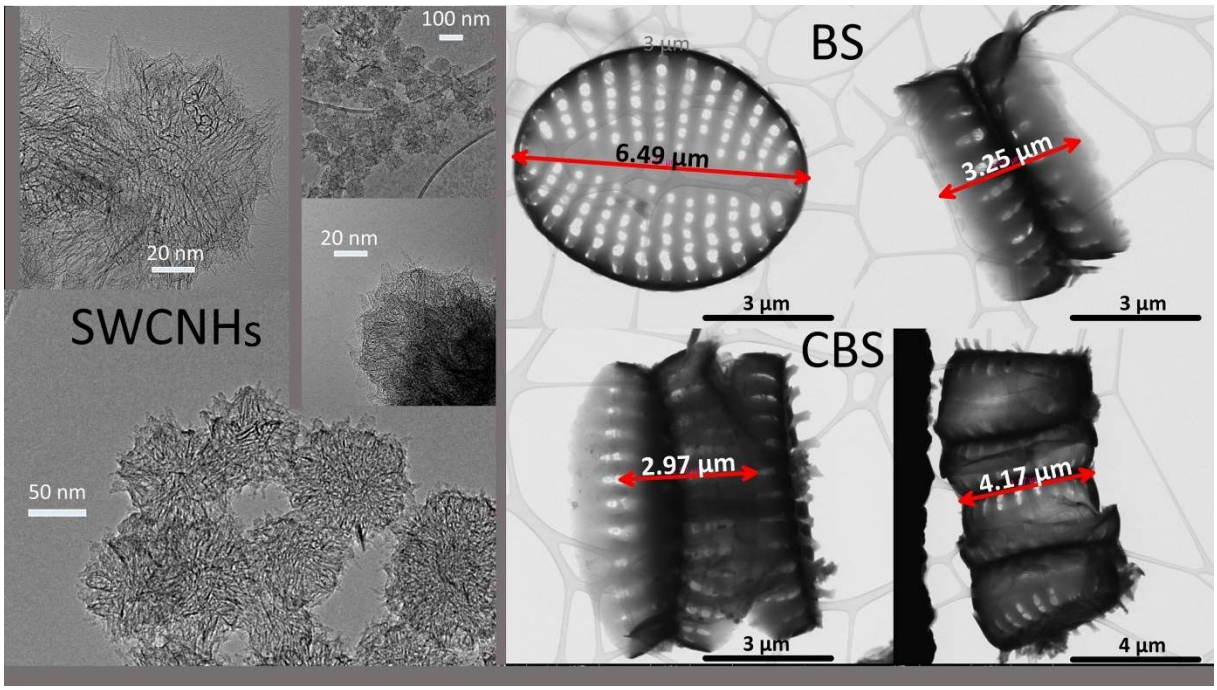

Figure 11. TEM images for the initial nano/micro materials.

Detailed analysis of TEM images of THV containing nano/micromaterials (Figs. 12 and 13) confirms the information provided above. One can observe single nanohorns, however, the majority of dahlia flowers are melted in THV (Fig. 12). A similar situation occurs for the remaining micromaterials – in this case also some regular shapes of uncovered diatoms are observed (Fig. 13). As it will be shown below, the presence of exposed nano/micro materials has a crucial influence on the values of WCA.

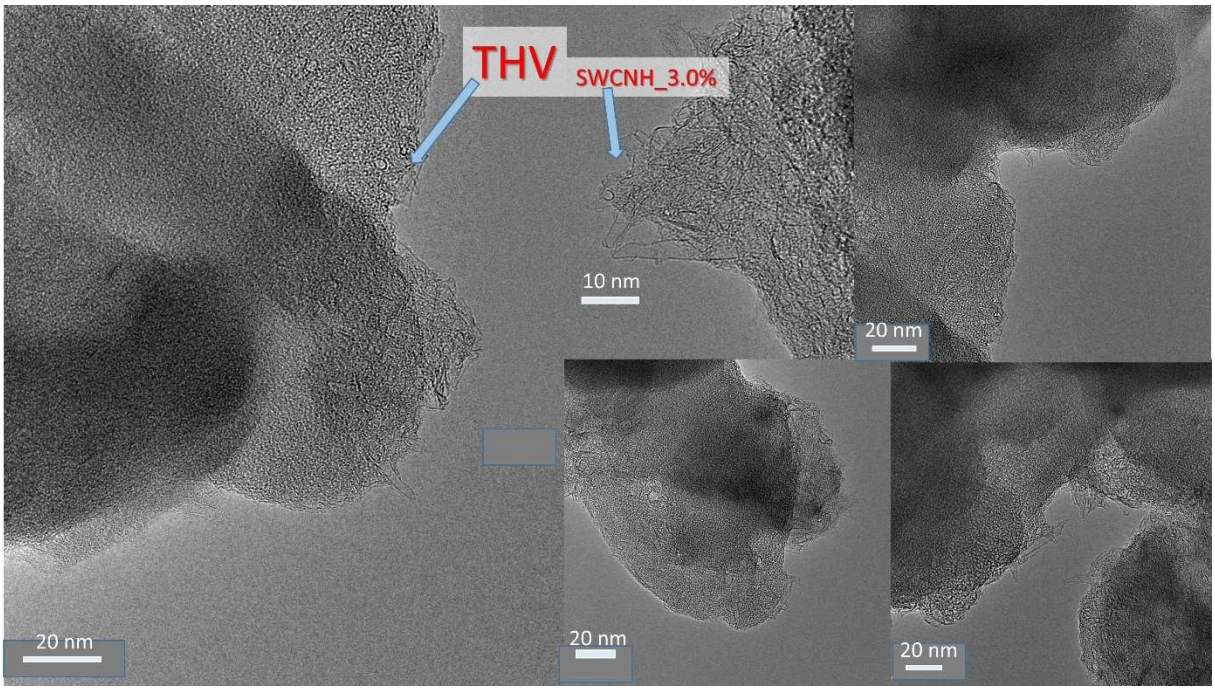

Figure 12. TEM images of $THV_{SWCNH\_3.0\%}$ system.

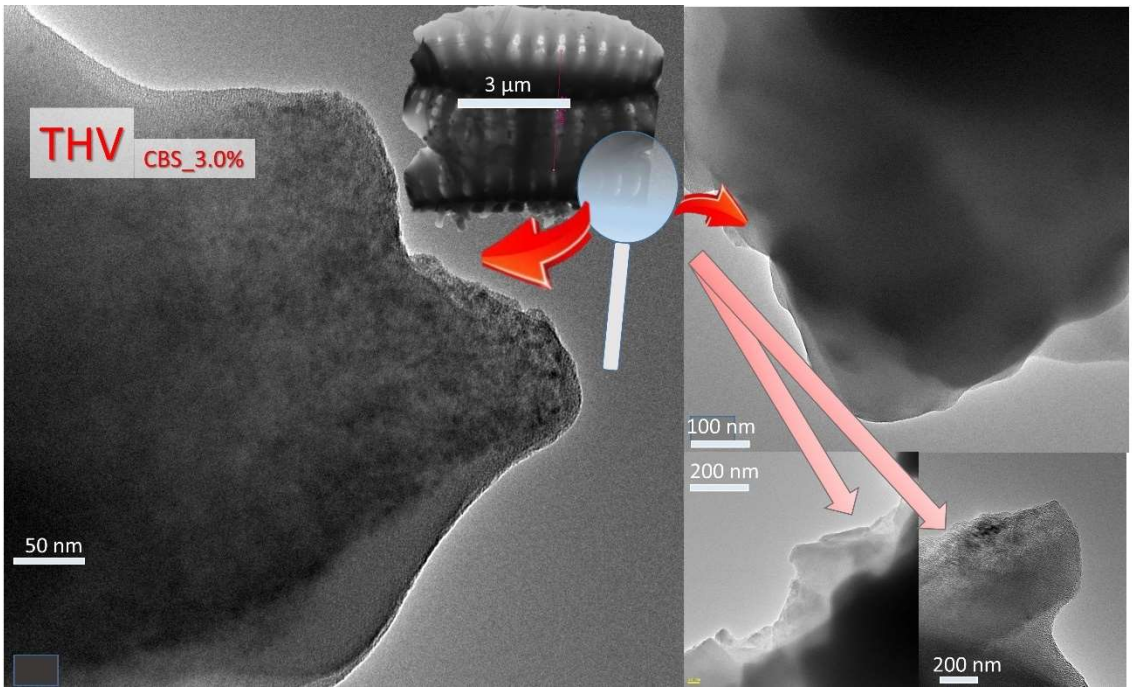

Figure 13. TEM images of $THV_{CBS\_3.0\%}$ system. Inset shows the image of a single CBS.

3.4. New forcefield for THV wetting, and wetting process in the light of MD results

Fig. 14A shows a snapshot from a simulation of a water droplet at the "flat" THV surface, while Fig. 14B displays the relevant contour of the drop. Simulated WCA equals 101.5°, which fully agrees with the experimental value of 101.6±2.2°. The details of the Lennard–Jones water-

surface interactions used in this simulation are collected in Fig. 16C. This force field can be applied for the simulation of THV wetting.

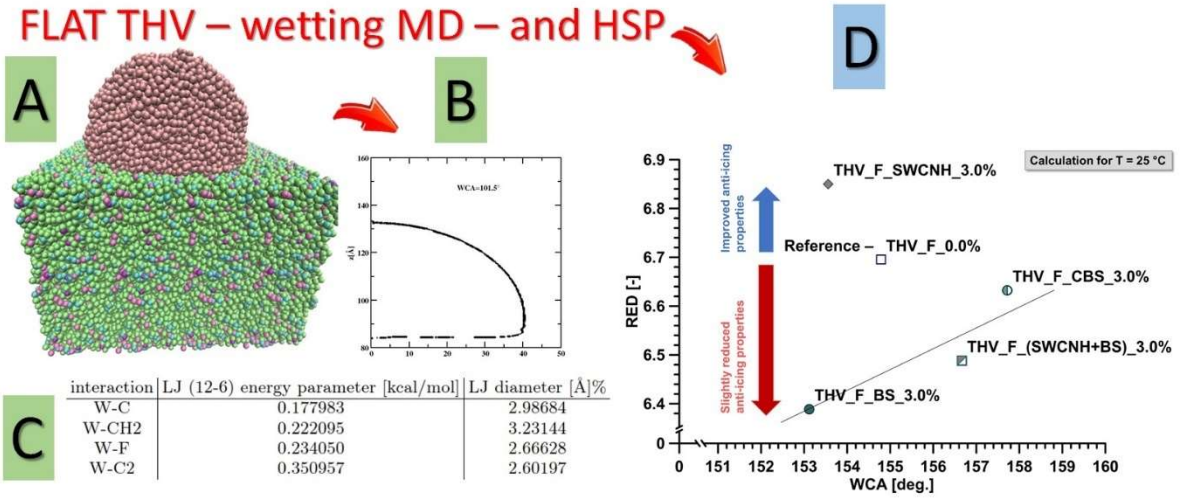

Figure 14. A snapshot of equilibrated 6000 water nanodroplet on THV surface at 25 °C (A), the equilibrium WCA (B), and the table (C) collecting water (W) – THV surface force field parameters (cutoff=10Å). The C2 type of atom denotes the carbon atom connected to the one fluorine atom in one HFF segment (-CF_2-$CFCF_3$-). The correlation between RED (calculated from HSP analysis) and WCA (measured on the outer upper skin surface of the sponge) is provided in (D).

Considering the influence of roughness, one can observe (Tab. 1) that MD simulation results predict the Cassie-Baxter effect, *i.e.*, the progressive rise in WCA value with the roughness observed for the experimental systems (Fig. 15).

Table 1. MD simulation results of WCA and freezing temperature for "flat"(THV_F) and rough (r) THV surfaces.

Sample	WCA [°]	Freezing Temperature [°C]
THV_F	101.5	-78.4±2.8
r05	103.3	-95.2±1.4
r10	106.6	-88.2±7.1
r15	113.2	-82.9±9.3

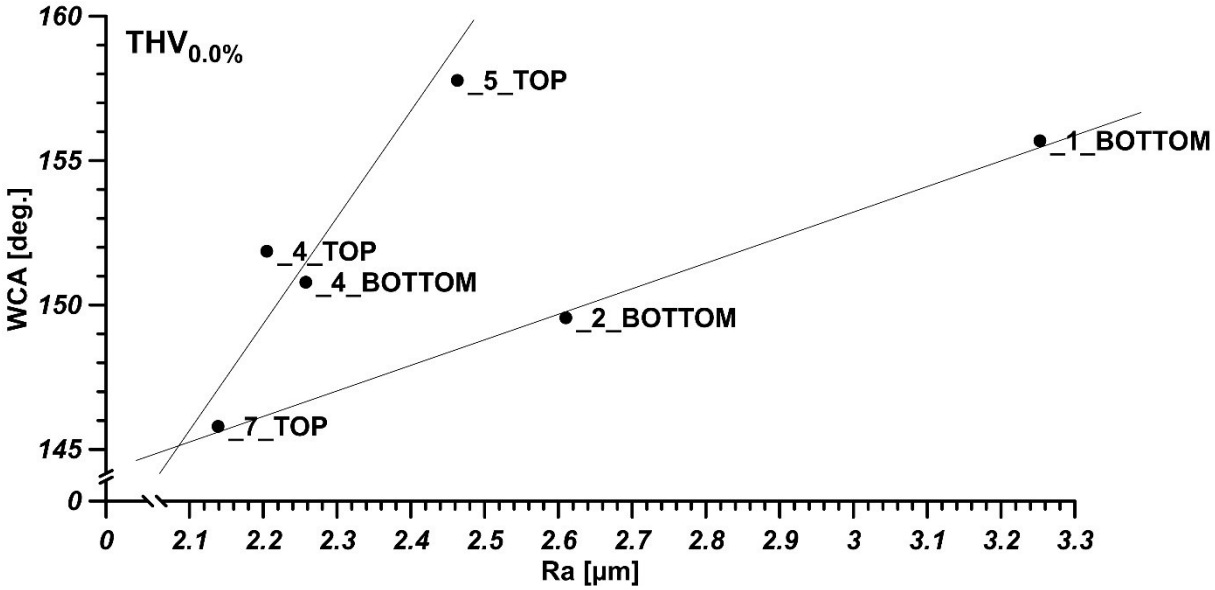

Figure 15. Experimental Relationship between R_a and WCA for THV.

3.5. Wetting in the light of HSP analysis

WCA value for the "flat" (reference) THV film having the same thickness as the studied sponges was equal to 101.6±2.2° (measured in this work). Thus, the creation of THV sponges increases the WCA value by about 50°. For the studied samples, we observe the average for all layers WCA, being the largest for $THV_{CBS\_3.0\%\_6\_TOP}$ (158.0°) and the smallest for $THV_{(SWCNH+BS)\_3.0\%\_1\_BOTTOM}$ (149.9°). Since, as it was concluded above from the results of TEM analysis, some nano/micromaterials are not fully covered by a polymer, the observed WCA values can result from hydrophobicity of SWCNHs and CBS and hydrophilicity of BS (see below). All surfaces are hydro/superhydrophobic due to the intrinsic hydrophobicity of THV.

HSP approach has been additionally implemented to analyze the wettability of sponges. In the first step of the analysis, the HSP parameters were calculated for the ambient atmosphere of sponges and water applied during the wettability studies *via* goniometric measurements (Fig. 14D). $THV_{SWCNH\_3.0\%}$ possesses the highest value of the RED as well as the largest distance in Hansen's sphere that is linked to the lowest affinity to water. The value of RED is equal to 6.85 and for the pure THV – 6.70, respectively.

Considering the average WCAs, the alteration is not substantial; $THV_{CBS\_3.0\%\_TOP}$ is characterized by the WCA equal to 158.0° and $THV_{(SWCNH+BS)\_3.0\%\_BOTTOM}$ by 149.9°. While those values may seem similar, they hold practical implications. The size of the fillers and their

impact on roughness, particularly the nanofiller SWCNHs, play a significant role in this context. However, the addition of micro-enhancers, despite being less hydrophobic, significantly increases the WCA. This is due to their much larger particle size. Their presence, especially in cases of settlement close to the surface, has a profound impact on the wettability feature, a crucial aspect of our research.

3.5. Freezing – MD simulation results

As demonstrated in [56], applied by us during MD simulation cooling rate enables the formation of ice. Crystalline structures can be described using local order parameters originally introduced by Steinhardt et al. [57] (see Eqs. S1-S5). Figure 16A shows the mean bond order parameters for the water drop on the THV surface calculated during the cooling process. A rapid increase in the value of the order parameters $<q_6>$, $<\bar{q}_4>$, and $<\bar{q}_6>$ signals the formation of ice. We note here that the droplet freezes at about -76 °C. This can be compared with the temperature of -72 °C for the homogeneous nucleation and with -61 °C for the heterogeneous nucleation at the graphene surface for this model [56]. Therefore the water freezing at the flat THV surface is moderately inhibited concerning the bulk freezing free and considerably inhibited concerning the graphene surface.

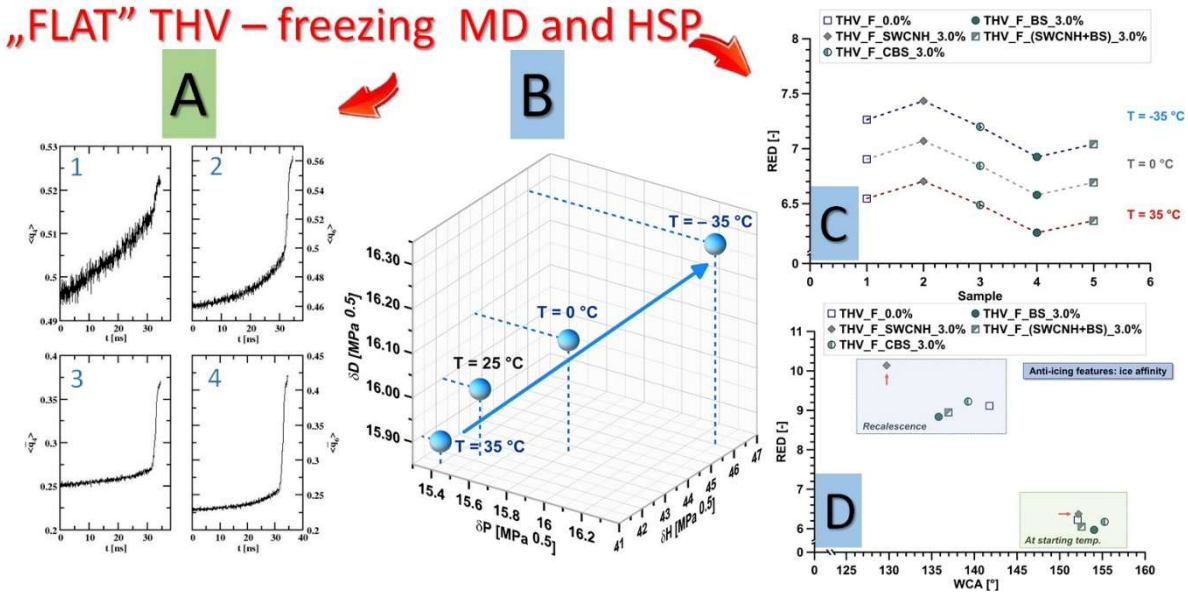

Figure 16. The mean bond order parameters for the water drop on the THV surface calculated during the cooling process (A 1-4). The changes in Hansen's parameters of water and ice in the Hansen's sphere (B). The evolution of the RED factor in the function of the temperature for the studied materials (C) and the relation between water contact angle and relative energy distance in the Hansen's sphere at the starting temperature of the measurement and recalescence phase (D).

Considering MD data for rough surfaces we observe the nonmonotonic behavior of freezing temperature with increasing roughness (Tab. 1, Fig.17A). Thi is in a good agreement with the experimental data (Fig. 17B), *i.e.*, also nonmonotonic behaviour is observed.

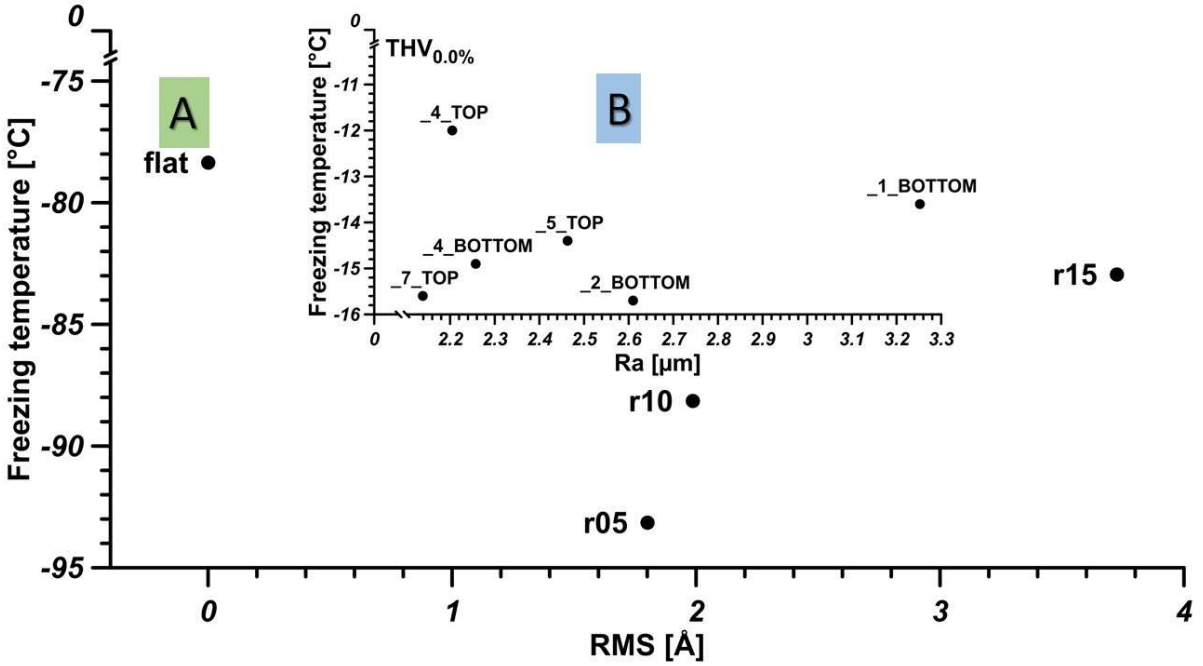

Figure 17. Simulated (A) and experimental (B) plots of freezing temperature vs roughness parameters.

We note that the small surface roughness leads to a suppression of the freezing temperature (Fig. 17A). This means that the ice formation on slightly rough THV surfaces is inhibited. However, as roughness increases, the freezing temperature increases as well. At first glance, this result may come as a surprise. However, we recall that in our simulation model the increase in the surface roughness is associated also with the decrease in the density. For wetting, both the surface roughness and the lower density lead to the increase in the contact angle (Table 1) in accordance with experimental data (Fig.15), *i.e.*, the two effect are synergistic. For freezing, the surface roughness and lowering of the density generate the opposite tendencies. At first, the lowering of the density leads to the decrease of the freezing temperature and for small surface rougness this effect dominates. The higher surface roughness eventually prevails and the freezing temperature increases in accordance with the experiment (Fig.17B).

3.6. Freezing in the light of Hansen Solubility Parameters analysis

A very interesting direct correlation has been found between the wettability of the materials and their affinity to water (Fig. 14D), which will determine the anti-icing properties at the lower range of temperatures (Fig. 16C). During the HSP calculation, the temperature factor is often not considered when determining R_a and RED parameters, which can lead to serious mistakes. For that reason, for the better understanding the anti-icing properties, the new parameters for a broad range of temperatures – coherent with the anti-icing analysis – were determined. The significant differences in the location of Hansen's sphere for water/ice were presented in Fig. 16B. The meaning of this plot is significant owing to that location of the sphere is changing substantially with the temperature. The real impact on the measurement of anti-icing feature is following. In the case of omitting the impact of the temperature on the HSP, it is impossible to get real response about the affinity of ice and investigated material of the surface. The most visible difference was observed in the hydrogen component of the HSP (δ_H) that is related to the polar character of the liquid. The value of the δ_H for water at the beginning of the measurements was equal to 42.6 $MPa^{0.5}$ and for the ice that value changed to 45.0 $MPa^{0.5}$ (Fig. 16B), accordingly. Then, the consequence of such noteworthy chances in the sphere location between water and ice was presented in Fig. 16C. This figure shows the impact of the material and water/ice temperature on the affinity between them. The measurements have been done according to the starting temperature and the temperature of recalescence, T_r. Moreover, a broader range of temperature was selected, considering the fundamental character of the research (Fig. 16B). It is justified that reducing the temperature enhances the anti-icing features for all of the investigated materials. The behaviors have been confirmed by the increase in the RED parameter, which confirms a lower affinity between the material and water or ice. In the case of the materials with the highest RED value, the water/ice will be removed most easily owing to the lack of minimal interactions. Among the synthesized materials, the $THV_{SWCNH\_3.0\%}$ was characterized by the lowest affinity to water or ice (Figs. 16 B-D). The value of RED is equal to 6.85 and for the pure THV 6.70, respectively. Considering the water contact angle, the alteration is not substantial; $THV_{SWCNH\_3.0\%}$ is characterized by the WCA equal to 153.51° and THV by 153.1°. While these values may seem similar, they hold practical implications. The size of the fillers and their impact on roughness, particularly the nanofiller SWCNH, play a significant role in this context. However, the addition of micro-enhancers, despite being less hydrophobic, significantly increases the water contact angle. This is due to their much larger particle size. Their presence, especially in cases of settlement close to the surface, has a

profound impact on the wettability feature, a crucial aspect of our research. A very interesting direct correlation has been found between the wettability of the materials and their affinity to water/ice, which will determine the anti-icing properties at the lower range of temperatures (Fig. 16D). In Fig.16D additionally the values were presented for two stages, at starting temperature of the measurement, and then at the recalescence temperature. That plot is again showing how the impact of the temperature is essential in the case of HSP and calculated factors based on the solubility parameters, *i.e.*, RED. Nevertheless, it is important to highlight that at both these temperature conditions, the $THV_{SWCNH\_3.0\%}$ sample is characterized by the best anti-icing properties.

3.7. Freezing – detailed insight into experimental results for sponges

Considering our data, we see that the addition of SWCNHs extends the time to recalescence (t_r) (see Fig. S12). Thus, the surfaces $THV_{SWCNH\_3.0\%\_TOP}$ (t_r = 250.0 s) and $THV_{SWCNH\_3.0\%\_BOTTOM}$ (t_r = 237.5 s) possess the most prospective anti-freezing properties. It should be noted that the largest t_r values were recorded for $THV_{SWCNH\_3.0\%\_3\_BOTTOM}$ (517.8 s), $THV_{SWCNH\_3.0\%\_2\_TOP}$ (432.2 s), and $THV_{SWCNH\_3.0\%\_7\_BOTTOM}$ (410.6 s). The average t_r values for $THV_{(SWCNH+BS)\_3.0\%\_TOP}$ (t_r = 225.3 s) are also large (in this series for the sample $THV_{(SWCNH+BS)\_3.0\%\_3\_TOP}$ t_r = 274.4 s). Compared to the sample containing only BS ($THV_{\_BS\_3.0\%\_TOP}$, average t_r = 128.4 s), the presence of SWCNHs increases average t_r values by about 110%!

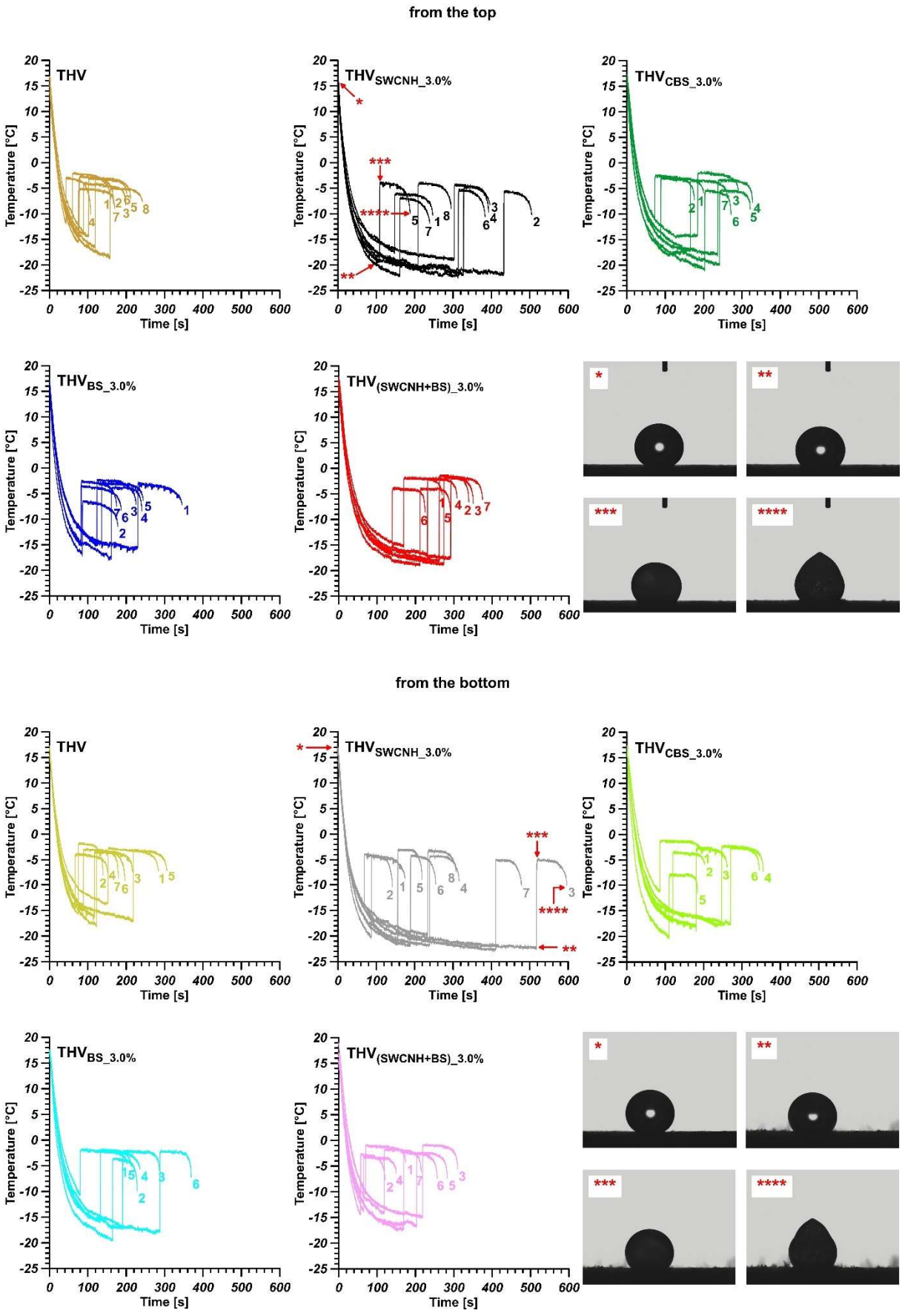

Figure 18. Temperature profiles during freezing on the cold plate measured for the "top" and

"bottom" samples. In both cases, as the fourth panels, are added snapshots for moments marked with stars on the example of the THV_SWCNH_3.0% sample

To summarize, the results for all "layered" samples we collect the data in Fig. 18 and S12. One can observe that the largest t_r values are observed for SWCNHs containing samples. Since the average freezing stage duration (defined previously [44] as the difference between the time necessary for the creation of a tip t_t and the time of recalescence t_r) is similar for all samples, we can conclude that crucial for inducing anti-freezing properties is the delay of the time of recalescence, as well as depletion of the recalescence temperature (see below). Summing up, to induce strong icephobicity a surface should not only possess as large WCA as possible but should also have a large heat capacity and small density, to avoid rapid heat transfer from a droplet. Taking into account a simple mass balance for a freezing droplet [43] (neglecting the evaporation process) one can write:

$$f_m = \frac{m_i}{m_d} = \frac{\Delta T}{L_f} \tag{1}$$

where: f_m is the mass fraction of ice in the droplet (equal to the ratio of mass of the ice and total mass of water in a droplet), ΔT is the difference between the temperature of the droplet at the subcooling stage and phase change, respectively (called subcooling degree of water droplet), L_f is the enthalpy of water solidification. Since the heat flux depends mainly on the temperature difference, density, and heat capacity, we expect that the introduction of nano/microfillers to THV sponges should increase heat capacity to diminish a heat flux from a plate to the droplet and, in this way, increase the time of recalescence. The data collected in Fig. 18 confirm this observation, *i.e.*, the lowest temperatures at the start of the freezing process are observed for SWCNHs-containing samples ($THV_{SWCNH\_3.0\%}$ and $THV_{(SWCNH+BS)\_3.0\%}$). This phenomenon leads to a quasi-linear correlation between the time of recalescence t_r and the recalescence temperature T_r (Fig. 19). It is worth to noting that the presence of SWCNHs filler gives a similar, but different, relationship from the others, indicating that SWCNHs are the best filler material here in the sought direction of extending the recalescence time.

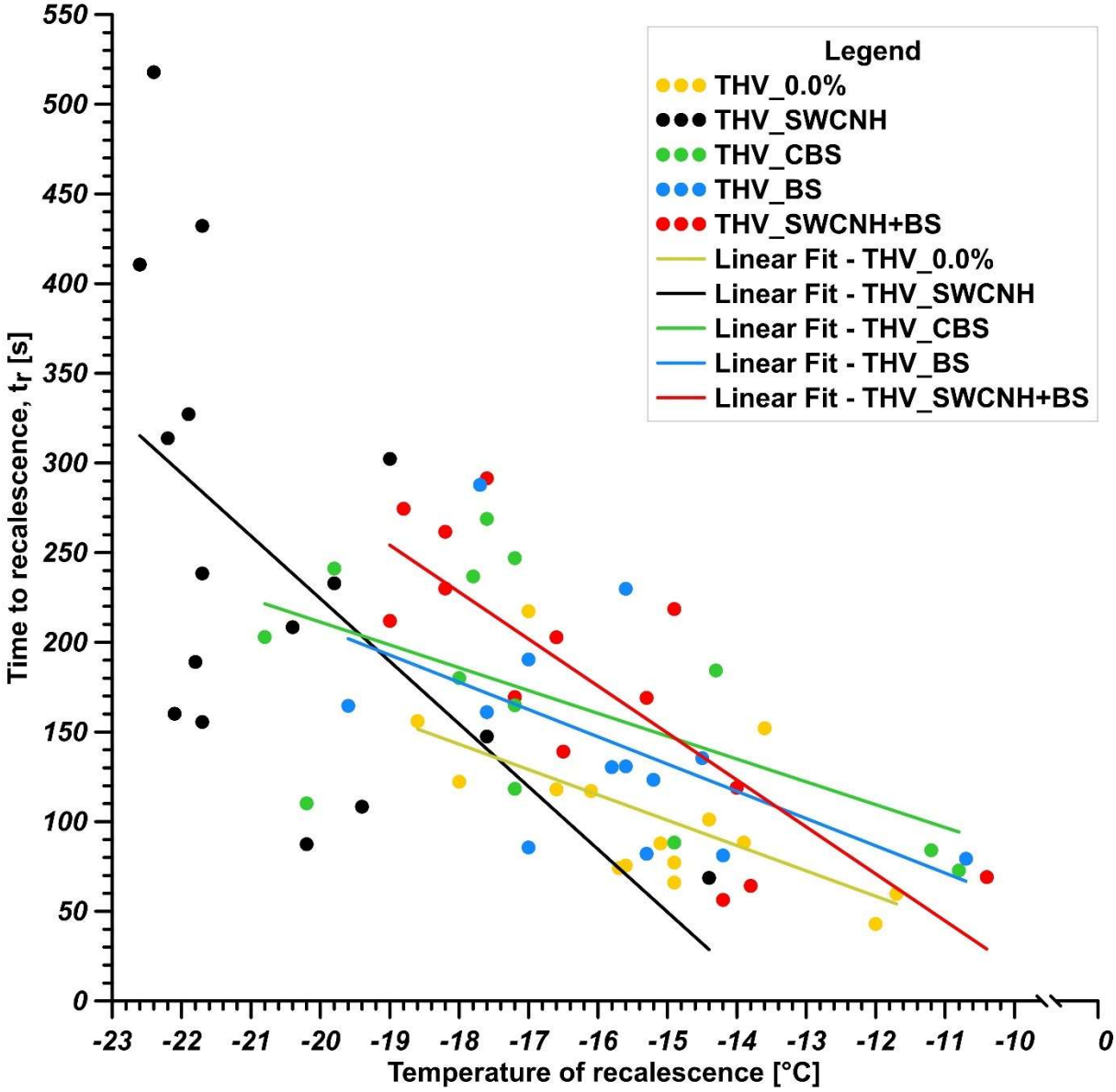

Figure 19. The correlation between the time to recalescence t_r and the temperature of recalescence T_r.

The above-shown correlation, as well as new correlations presented later in this paper, can be useful during the derivation of the model relating the properties of sponges with anti-icing features. Those relationshipswill be the subject of our future studies.

3.8. Freezing – experimental results for "flat" surfaces

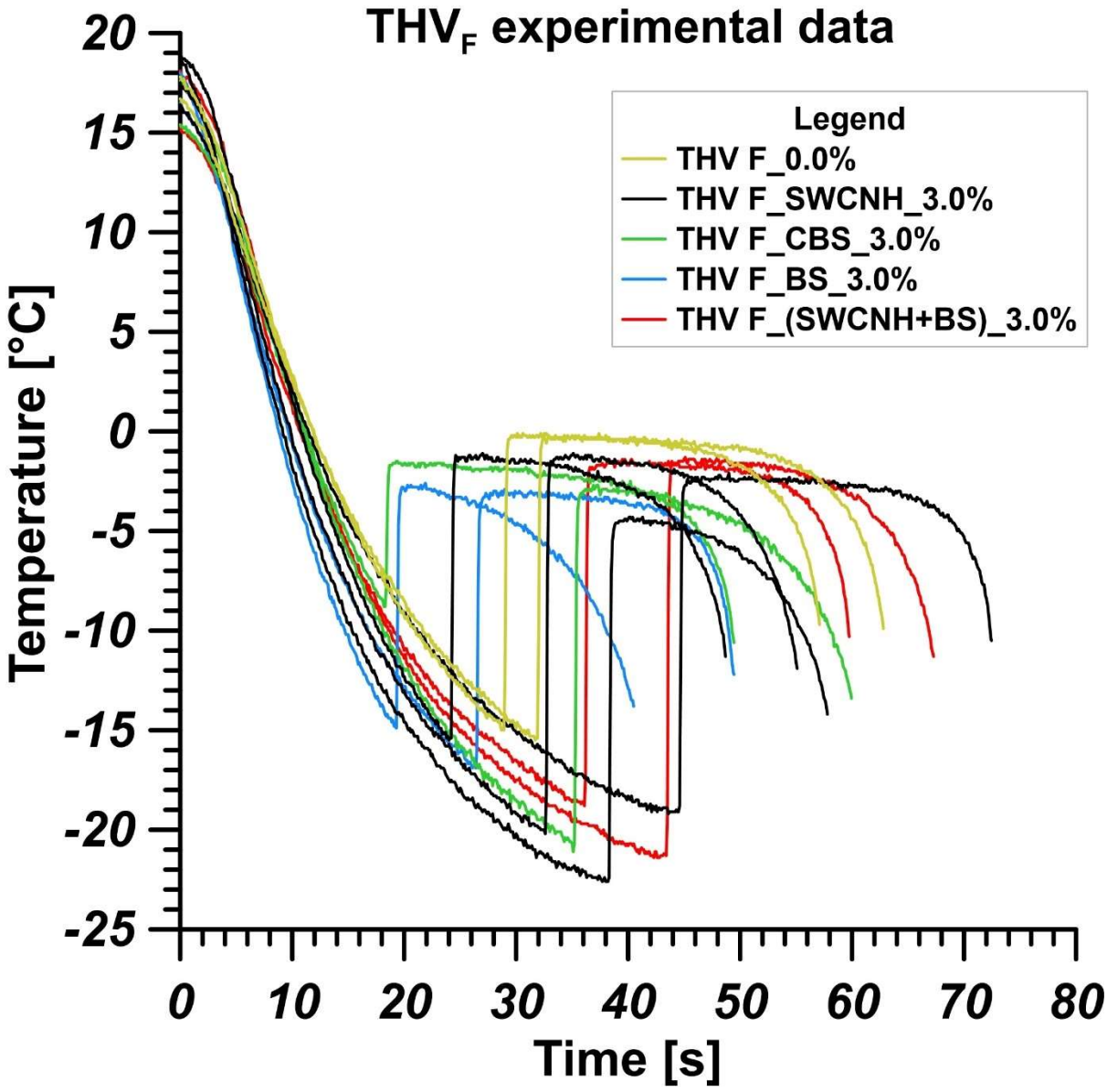

Figure 20. Temperature profiles during freezing on the cold plate measured for the "flat samples".

The first thing one can see in Fig. 20 is the shorter times necessary for the droplets to freeze compared to the sponges (Fig. 18). Much smaller scatter of values on the time axis is also visible. In fact, if we consider Eq. (1) and the accompanying discussion, we can, at the first approximation, explain the obtained results by the difference in heat flux. Since the system is nonporous (no air in pores), heat flux is larger, therefore the freezing time is shorter. It was shown recently by numerical analysis that thermal conductivity for cellular materials decreases with porosity [58]. The analysis of WCA values for "flat" surfaces shows that there are no such huge differences in WCA values as observed for sponges (the smallest WCA = 95.5° was

recorded for the $THV_{F\_(BS)\_3.0\%}$ and the largest, 108.8° for the sample $THV_{F\_(SWCNH)\_3.0\%}$). The observed correlation between RED and WCA (see Fig. 21A) is also interesting.

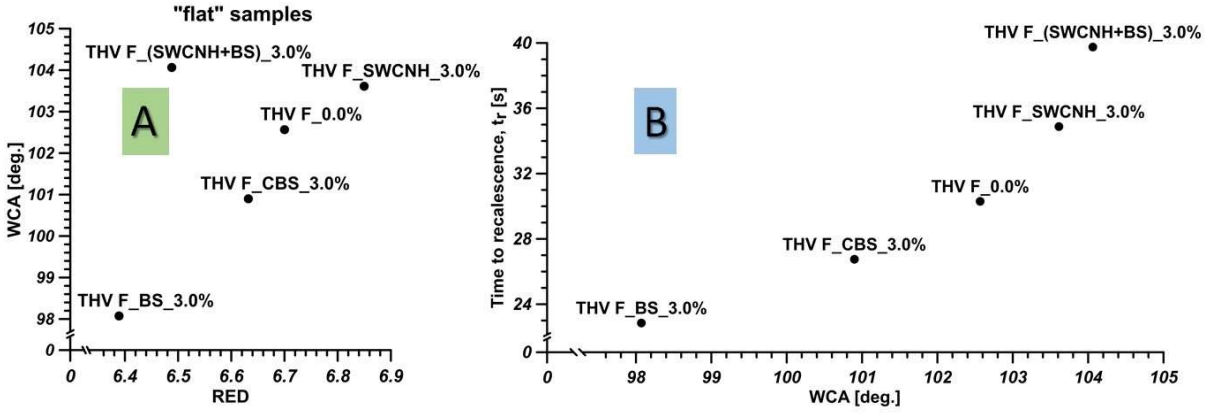

Figure 21. The correlations between RED and WCA (A) and between WCA and averaged time to recalescence t_r (B) for "flat" surfaces.

One can see that one of the systems ($THV_{(SWCNH+BS)\_3.0\%\_f}$) does not follow this correlation. This is due to the fact that RED is strongly influenced by silica, but it is heavier and the skin surface of the sponge contains mainly carbon nanohorns, and these, as we know, give a large WCA. What is very important, the addition of nano/micro fillers for "flat" surfaces not always improve anti-icing properties. Thus, for pure nonporous THV, the recalescence time was equal to 28.8 s and the recalescence temperature -13.7 °C. The addition of two fillers – BS and CBS slightly shortened the time to recalescence and this is probably caused by the decrease in WCA compared to pure, "flat" THV. The time to recalescence t_r is correlated with WCA (Fig. 21B).

Summing up, the addition of micro fillers, leading to slight hydrophilization of "flat" THV surface causes a shortening of the time to recalescence t_r. In the case of "flat" surfaces, the smallest recalescence temperature T_r and the longest time to recalescence t_r are observed for the samples containing SWCHs. Considering our freezing results, it is important to mention the study by Heydari et al. [41] who concluded that freezing delay time (in our study we use the time of recalescence t_r and freezing stage duration $t_t - t_r$, respectively) is similar for different studied surfaces (Wenzel, smooth, superhydrophobic) and smooth as well as Wenzel surfaces delayed freezing a bit stronger. The results in our study show that for "flat" surfaces this is true, since we observe the maximum drop in recalescence temperature (for $THV_{SWCNH\_3.0\%\_f}$)

compared to flat THV sample by about ca. 7 °C, with the elongation of time to recalescence t_r by ca. 6 s. However, the creation of sponges, based on the procedure presented in this study, is an excellent strategy for inducing more pronounced anti-icing features. On the other hand, since the sponges are not as mechanically resistant as bulk solids, it is important to check how the addition of nano/microfillers changes the mechanical properties (see below).

The results of resistivity for "flat" samples show that Joule effect can be applied not only for the samples containing SWCNHs but CBS as well (Tab. S2).

3.7. Mechanical properties results in relation to anti-freezing properties

Mechanical properties are very important in the practical application of anti-icing materials [59]. Generally, considering sponges, to change the desired properties, they are often functionalized by introducing various types of additives such as graphene oxide, [19] carbon black nanoparticles [31], cellulose fibers [60], multi-walled CNTs [61] and other types of carbon materials or mineral nanoparticles [62,63].

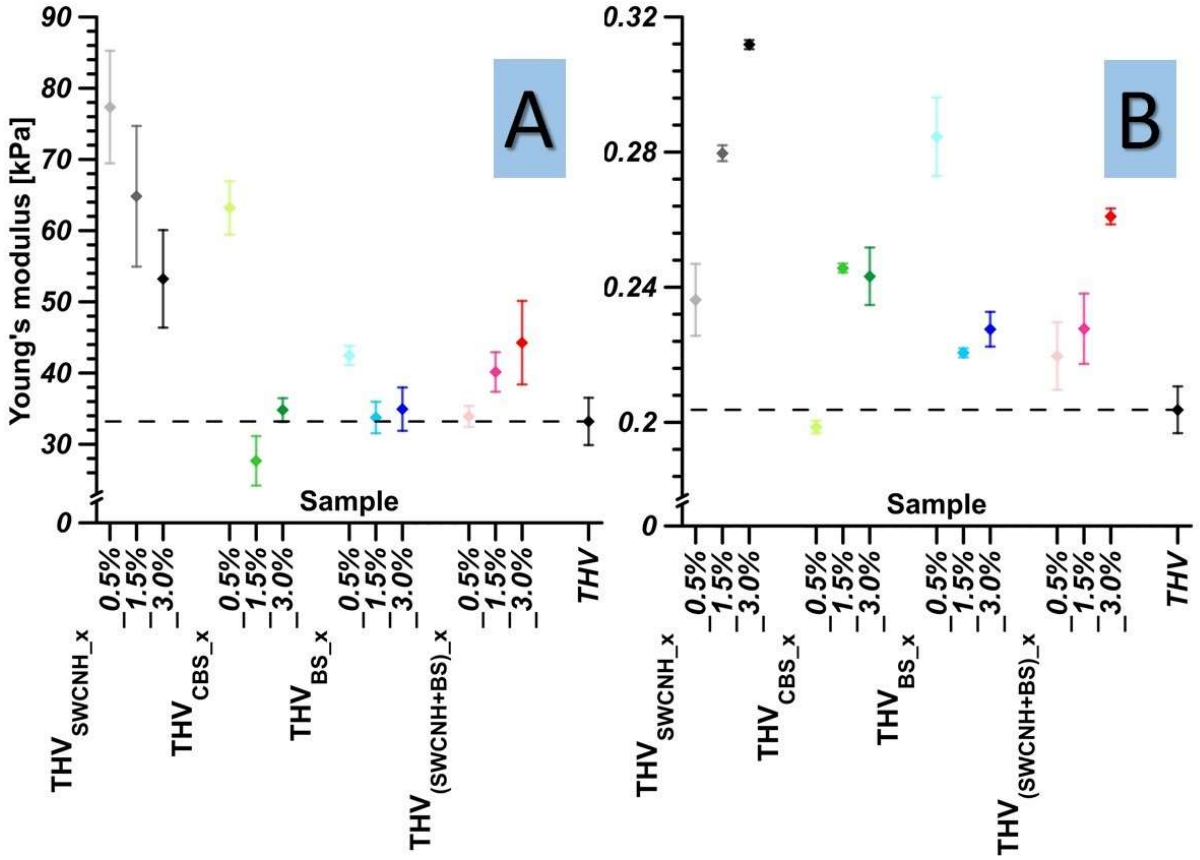

Figure 22. Young's modulus values determined for studied sponges (A) and compressive stress results for 80% of deformation for studied sponges (B).

Fig. 22A shows the values of YM calculated for particular composites containing 0.5%, 1.5%, and 3% of the fillers discussed. It is well known that the longitudinal modulus of elasticity (E), also called the modulus of linear deformation, is one of several properties that affect elasticity, and it characterizes the resistance of the material to elastic elongation. The higher the value of the E modulus, the less the material deforms. The introduction of 0.5% fillers in the form of SWCNHs, CBS, and BS into the polymer matrix causes a significant increase in the value of YM, which indicates an increase in the stiffness of the obtained sponges. At the same time, it should be noted that the addition of larger amounts of the above-mentioned fillers (1.5% and 3.0%) reduces the E values. However, for samples containing SWCNHs, YM value is still higher than for the pure polymer, while in the case of materials containing 1.5% and 3.0% BS and CBS, it drops to the level of a pure polymer sample or even slightly more, reaching lower values. The obtained results indicate that the introduction of small amounts of these fillers causes an increase in the tangent of the stress-strain curve angle. However, the addition of 1.5% and 3.0% of SWCNHs, CBS, and BS fillers may significantly disturb the formation of a uniform porous structure and a uniform distribution of the filler in the polymer matrix. This results in a

lower value of YM compared to the samples containing 0.5% of additives. The opposite tendency to the above-mentioned composites is observed for materials containing two fillers: SWCNHs and BS. On introducing these compounds, YM value increases with the amount of the filler incorporated into the polymer matrix.

Another parameter analyzed during the mechanical tests was compressive stress, i.e., the stress occurring in the material under compression at 80% deformation (Figure 22B). Just as YM provides information about the stress during the first stage of compression, compressive stress indicates the force that is necessary to obtain a particular degree of deformation. Both compressive stress values and trends vary significantly depending on the type and the amount of the filler used. In the case of materials containing SWCNHs and a mixture of SWCNHs and BS fillers, the compressive stress increases with the amount of added fillers. A similar effect of additives in the form of alginate and activated carbon on the compressive stress of polyurethane-based sponges was observed by Mallakpour and Behranvand [18]. This effect has not been recorded in the case of materials with the addition of BS only, where the highest value was obtained for the sample incorporating 0.5% of the filler, and for materials with the addition of CBS, where the lowest compressive stress value was recorded for the sample with 0.5% of the filler – a value lower than measured concerning the pure material. The obtained results are reflected in the value of the maximum force during compression, with Fig. 23 depicting the change in values during subsequent cycles of compression.

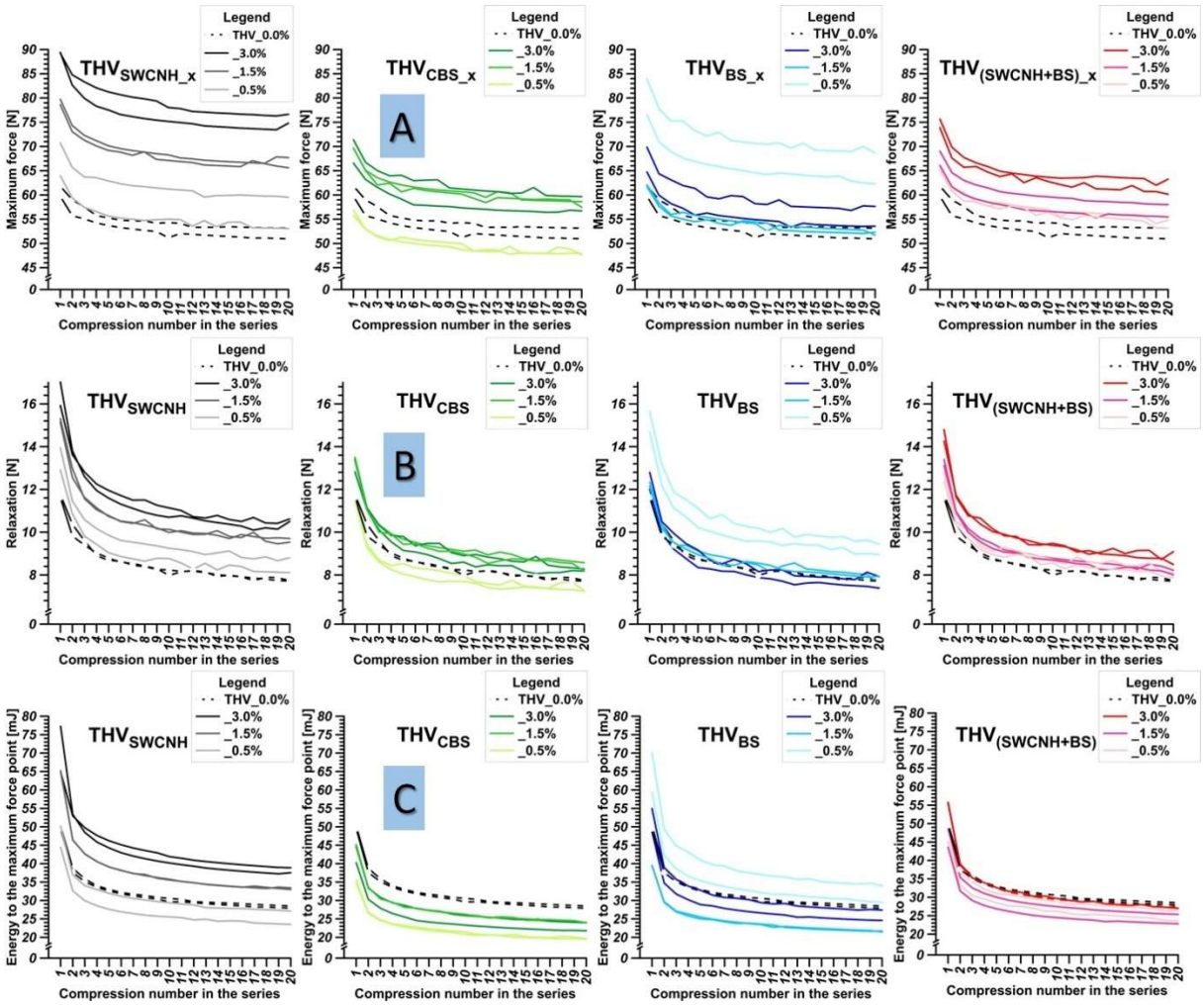

Figure 23. Maximum force during compression cycles (A), relaxation results for studied samples (B), and energy to the maximum force during compression (C).

In the case of the maximum force recorded concerning individual compression cycles, a decrease in its value is observed after the first two compression cycles. However, during subsequent compression cycles, the maximum force remains almost unchanged (Fig. 23A), which indicates elastic deformations of the tested materials [64]. Similar behavior was observed in the case of sponges described in our previous work, where the influence of the type of solvent on the properties of sponges formed from pure THV was analyzed [36]. It should be noted that for almost all materials, except the sample containing 0.5% CBS, the maximum force values are higher than the maximum force values obtained for the pure polymer. Moreover, it was noted that an introduction of 0.5% BS into the polymer matrix leads to a significant increase in the value of the maximum force, while further addition of BS leads to a decrease in the value of the maximum force. These observations suggest that this filler is subject to sedimentation.

These assumptions are consistent with YM values, which, for samples with 1.5% and 3.0% of BS filler, are close to the value obtained for the pure polymer.

Another parameter analyzed during cyclic compression tests was relaxation. During 20 compression cycles, relaxation was observed for 30 seconds for each cycle (Fig. 23B). This study allowed for a comparison of the effect of individual additives on the movement of THV polymer macromolecule chains. The obtained results prove that the addition of SWCNHs has the greatest impact on the relaxation process, while the incorporation of CBS into the polymer matrix has the least. Moreover, it should be stressed that the same direction of change observed for relaxation can also be observed in the case of maximum force changes.

However, the same trends – as in the case of the maximum force and relaxation values – have not been observed concerning the calculated energy (Fig. 23C). A high value of maximum force might seem to guarantee a high value of the absorbed energy. A high energy value indicates a large area under the curve, which implies that significant stress values are obtained even when only a small deformation of the material occurs. Therefore, in the case of materials that were characterized by higher values of maximum force than the reference sample, and at the same time, their energy remained at a lower level compared to the control sample, it can be assumed that in the first seconds of the compression process, the stress values reached low values. Such observation suggests that the fillers were partially sedimented during the formation of the sponges, which could translate into lower stress values in the initial phase of the test and higher values when the predetermined 80% deformation was achieved. This phenomenon was observed with most of the tested materials, except for samples containing 1.5% and 3.0% SWCNHs, and 0.5% biosilica. The conducted experiments indicate that, depending on the type and amount of the introduced additive, different effects can be achieved depending on the needs. Among the analyzed materials, sponges containing SWCNHs seem to be the most promising. This filler causes the obtained materials to stand out in terms of mechanical properties compared to the other additives.

In our previous study [47] it was concluded that freezing stage duration correlates with YM (generally, it decreases with the rise in YM). It was seen (see Fig. 11E in [47]) that this relation is not valid for all samples in a series, but occurs for similar materials. The same situation is observed for the samples studied in this paper (Fig. 24A), namely, linear dependence is observed for the initial THV sponge and SWCNH-containing sponges, but not for the sponges containing micromaterials.

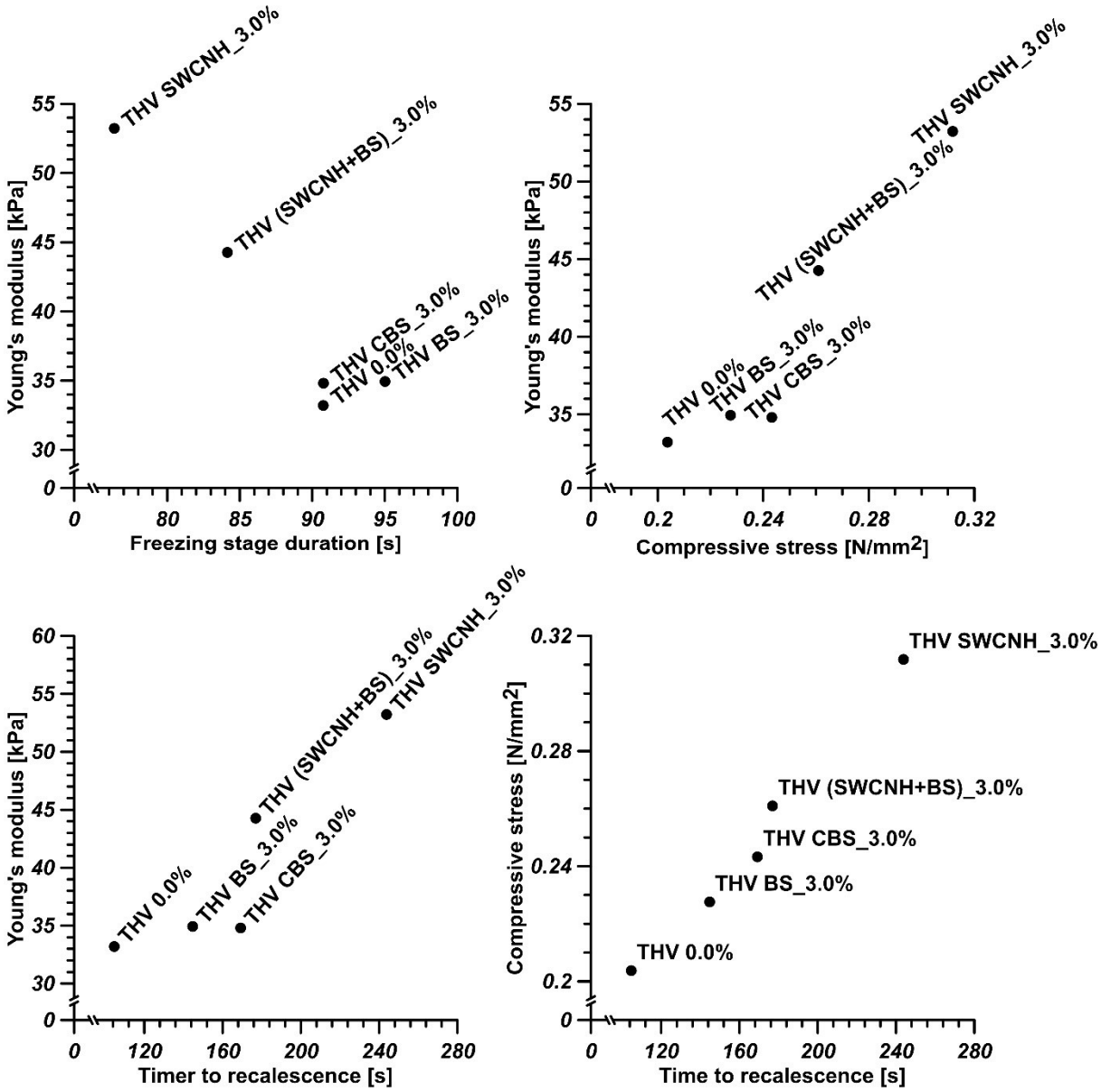

Figure 24. The correlations between freezing stage duration $t_t - t_r$ and time to recalescence t_r and mechanical parameters, i.e., Young's modulus (A, C) and compressive stress (D) of studied "bulk" sponges. The correlation between the both mechanical properties is also shown (B).

However, as it is seen from Fig. 24C that the time to recalescence t_r increases with the values of YM as well as with compressive stress for the studied materials (by the way both values are correlated for the studied samples – see Fig. 24B). Although the relation between YM and thermal conductivity is not obvious, there are some reports showing the rise in thermal conductivity with the rise in YM for some polymers [65] or buckypapers [66] and the decrease in thermal conductivity with the development of porosity [58]. On the other hand, thermal

conductivity is strongly affected by porosity [67]. This subject needs further studies and the results will be reported.

Our results show that the rise in YM as well as the rise in compressive stress causes the rise in the recalescence time t_r. The largest values of both mechanical properties are observed for SWCNH-containing sponges, while the lowest ones for the initial THV and the sponges containing BS and CBS (similar values). Summing up, the introduction of SWCNHs to THV causes not only the improvement of mechanical properties but also the improvement of anti-icing properties, especially to the stage of recalescence. At the same time, small deterioration is observed considering the freezing stage duration. Fortunately, after the recalescence step, the Joule heating can be switched on.

4.0. Conclusions

A nano/micro modified THV polymer of various morphological and 3D variants was studied as an anti-icing material. We have cross-verified the properties of foams, "layered" surfaceas as well as "flat" ones. All studied nano/micro fillers improve thermal and mechanical properties of the sponges. Among fillers, SWCNHs emerge as the most suitable and tunable for inducing anti-icing properties by enhancing time to recalescence as well as decreasing the droplet freezing temperature. Application of MD simulations and the HSP analysis allow to show new correlations describing freezing on a cold plate as well as the influence of roughness on the process. The obtained results can be important for the creation of a new simple model describing this important everyday life process.

Acknowledgements: This paper is dedicated to the memory of prof. Stefan Sokołowski who passed away on 24.06.2024. A.P.T and S.B. gratefully acknowledge the financial support from NCN Opus 22 project: UMO-2021/43/B/ST5/00421. S.B. also acknowledges the supporting actions from EU's Horizon 2020 ERA-Chair project ExCEED, grant agreement No. 952008. P.B. acknowledges CPU time from CI TASK Gdańsk, Poland, under Grant PT01162, and is grateful to L.G. MacDowell and P. Llombart for enlightening discussions. Thermal analyses were performed in the Centre of Synthesis and Analysis BioNanoTechno of the University of Bialystok. The equipment in the Centre was funded by the EU as a part of the Operational Program Development of Eastern Poland 2007-2013. projects: POPW.01.03.00-20-034/09-00 and POPW.01.03.00-20-004/11.

References

[1] Huang J, Peng Z, Zhang B, Yao Y, Chen S. A Flexible and High-Efficient Anti-Icing/Deicing Coating Based on Carbon Nanomaterials. ACS Appl Mater Interfaces 2024;16:44210–24. https://doi.org/10.1021/acsami.4c06682.

[2] Hori K, Yamada Y, Momma T, Noda S. High-energy density Li Si-S full cell based on 3D current collector of few-wall carbon nanotube sponge. Carbon 2020;161:612–21. https://doi.org/10.1016/j.carbon.2020.02.004.

[3] Huang L, Chen J, Xu Y, Hu D, Cui X, Shi D, et al. Three-dimensional light-weight piezoresistive sensors based on conductive polyurethane sponges coated with hybrid CNT/CB nanoparticles. Applied Surface Science 2021;548:149268. https://doi.org/10.1016/j.apsusc.2021.149268.

[4] Luo Y, Xiao Q, Li B. Highly compressible graphene/polyurethane sponge with linear and dynamic piezoresistive behavior. RSC Adv 2017;7:34939–44. https://doi.org/10.1039/C7RA03922K.

[5] Fu Y, Zhao G, Zhao H, Wan Z, Jia W. Investigation into a Conductive Composite Matrix Based on Magnetically Sensitive Flexible Sponges. Ind Eng Chem Res 2020;59:15967–78. https://doi.org/10.1021/acs.iecr.0c02239.

[6] Zhang F, Feng Y, Qin M, Gao L, Li Z, Zhao F, et al. Stress Controllability in Thermal and Electrical Conductivity of 3D Elastic Graphene-Crosslinked Carbon Nanotube Sponge/Polyimide Nanocomposite. Adv Funct Mater 2019;29:1901383. https://doi.org/10.1002/adfm.201901383.

[7] Chen Y, Yang Y, Xiong Y, Zhang L, Xu W, Duan G, et al. Porous aerogel and sponge composites: Assisted by novel nanomaterials for electromagnetic interference shielding. Nano Today 2021;38:101204. https://doi.org/10.1016/j.nantod.2021.101204.

[8] Chen W, Duan W, Liu Y, Wang Q, Qi F. Facile Fabrication of Multifunctional Polymer Composites Based on Three-Dimensional Interconnected Networks of Graphene and Carbon Nanotubes. Ind Eng Chem Res 2019;58:21531–41. https://doi.org/10.1021/acs.iecr.9b04854.

[9] Shen B, Li Y, Zhai W, Zheng W. Compressible Graphene-Coated Polymer Foams with Ultralow Density for Adjustable Electromagnetic Interference (EMI) Shielding. ACS Appl Mater Interfaces 2016;8:8050–7. https://doi.org/10.1021/acsami.5b11715.

[10] Arefpour A, Kasiri-Asgarani M, Monshi A, Karbasi S, Doostmohammadi A, Rostami S. *In vitro* bioactivity of baghdadite-coated PCL –graphene nanocomposite scaffolds: mechanism of baghdadite and apatite formation. Materials Technology 2021;36:761–70. https://doi.org/10.1080/10667857.2020.1794281.

[11] Jahandideh H, Nguyen QA, Tufenkji N. Polymer-Free Emulsion-Templated Graphene-Based Sponges for Contaminant Removal. ACS Appl Mater Interfaces 2020;12:52095–103. https://doi.org/10.1021/acsami.0c11895.

[12] Affonso LN, Marques JL, Lima VVC, Gonçalves JO, Barbosa SC, Primel EG, et al. Removal of fluoride from fertilizer industry effluent using carbon nanotubes stabilized in chitosan sponge. Journal of Hazardous Materials 2020;388:122042. https://doi.org/10.1016/j.jhazmat.2020.122042.

[13] Mallakpour S, Behranvand V. Modification of polyurethane sponge with waste compact disc-derived activated carbon and its application in organic solvents/oil sorption. New J Chem 2020;44:15609–16. https://doi.org/10.1039/D0NJ02839H.

[14] Yap PL, Auyoong YL, Hassan K, Farivar F, Tran DNH, Ma J, et al. Multithiol functionalized graphene bio-sponge via photoinitiated thiol-ene click chemistry for efficient heavy metal ions adsorption. Chemical Engineering Journal 2020;395:124965. https://doi.org/10.1016/j.cej.2020.124965.

[15] Ahmed RMG, Anis B, Khalil ASG. Facile surface treatment and decoration of graphene-based 3D polymeric sponges for high performance separation of heavy oil-in-water emulsions. Journal of Environmental Chemical Engineering 2021;9:105087. https://doi.org/10.1016/j.jece.2021.105087.

[16] Chatterjee S, Doshi P, Kumaraswamy G. Capillary uptake in macroporous compressible sponges. Soft Matter 2017;13:5731–40. https://doi.org/10.1039/C7SM00826K.
[17] Li B, Liu X, Zhang X, Zou J, Chai W, Xu J. Oil-absorbent polyurethane sponge coated with KH-570-modified graphene. J Appl Polym Sci 2015;132:n/a-n/a. https://doi.org/10.1002/app.41821.
[18] Mallakpour S, Behranvand V. Polyurethane sponge modified by alginate and activated carbon with abilities of oil absorption, and selective cationic and anionic dyes clean-up. Journal of Cleaner Production 2021;312:127513. https://doi.org/10.1016/j.jclepro.2021.127513.
[19] Feng L, Gao Y, Hou X, Dan H, Wei Y, Yin W, et al. Phytic acid and graphene oxide functionalized sponge with special-wettability and electronegativity for oil-in-water emulsion separation in single-step. Journal of Hazardous Materials 2022;435:129003. https://doi.org/10.1016/j.jhazmat.2022.129003.
[20] Pinto J, Athanassiou A, Fragouli D. Effect of the porous structure of polymer foams on the remediation of oil spills. J Phys D: Appl Phys 2016;49:145601. https://doi.org/10.1088/0022-3727/49/14/145601.
[21] Gao Q, Tran T, Liao X, Rosenfeldt S, Gao C, Hou H, et al. Ultralight Heat-Insulating, Electrically Conductive Carbon Fibrous Sponges for Wearable Mechanosensing Devices with Advanced Warming Function. ACS Appl Mater Interfaces 2022;14:19918–27. https://doi.org/10.1021/acsami.2c04136.
[22] Guan H, Dai X, Ni L, Hu J, Wang X. Highly Elastic and Fatigue-Resistant Graphene-Wrapped Lamellar Wood Sponges for High-Performance Piezoresistive Sensors. ACS Sustainable Chem Eng 2021;9:15267–77. https://doi.org/10.1021/acssuschemeng.1c05401.
[23] Wu X, Han Y, Zhang X, Zhou Z, Lu C. Large-Area Compliant, Low-Cost, and Versatile Pressure-Sensing Platform Based on Microcrack-Designed Carbon Black@Polyurethane Sponge for Human-Machine Interfacing. Adv Funct Mater 2016;26:6246–56. https://doi.org/10.1002/adfm.201601995.
[24] Liu W, Liu N, Yue Y, Rao J, Luo C, Zhang H, et al. A flexible and highly sensitive pressure sensor based on elastic carbon foam. J Mater Chem C 2018;6:1451–8. https://doi.org/10.1039/C7TC05228F.
[25] Zhang L, Feng L, Gu X, Zhang C. Additive-free, robust and superelastic dual-network graphene/melamine composite sponge for motion sensing. J Appl Polym Sci 2021;138:50788. https://doi.org/10.1002/app.50788.
[26] Zhang S, Wang S, Wang Y, Fan X, Ding L, Xuan S, et al. Conductive shear thickening gel/polyurethane sponge: A flexible human motion detection sensor with excellent safeguarding performance. Composites Part A: Applied Science and Manufacturing 2018;112:197–206. https://doi.org/10.1016/j.compositesa.2018.06.007.
[27] Zhang Y, Zhen Z, Zhang Z, Lao J, Wei J, Wang K, et al. In-situ synthesis of carbon nanotube/graphene composite sponge and its application as compressible supercapacitor electrode. Electrochimica Acta 2015;157:134–41. https://doi.org/10.1016/j.electacta.2015.01.084.
[28] Dai Z, Weng C, Liu L, Hou Y, Zhao X, Kuang J, et al. Multifunctional Polymer-Based Graphene Foams with Buckled Structure and Negative Poisson's Ratio. Sci Rep 2016;6:32989. https://doi.org/10.1038/srep32989.
[29] Zheng X, Zhang H, Liu M, Zhou X, Wang H, Jiang R. Porous sponge with surface modified for superhydrophobic/superoleophilic and special functionalization. J Polym Res 2022;29:237. https://doi.org/10.1007/s10965-022-03031-4.
[30] Zhang B-X, Hou Z-L, Yan W, Zhao Q-L, Zhan K-T. Multi-dimensional flexible reduced graphene oxide/polymer sponges for multiple forms of strain sensors. Carbon 2017;125:199–206. https://doi.org/10.1016/j.carbon.2017.09.055.
[31] Cheong JY, Benker L, Zhu J, Youn D-Y, Hou H, Agarwal S, et al. Generalized and feasible strategy to prepare ultra-porous, low density, compressible carbon nanoparticle sponges. Carbon 2019;154:363–9. https://doi.org/10.1016/j.carbon.2019.08.021.

[32] Sun Y, Chen L, Yu J, Yoon B, Lee SK, Nam J-D, et al. Lightweight graphene oxide-based sponges with high compressibility and durability for dye adsorption. Carbon 2020;160:54–63. https://doi.org/10.1016/j.carbon.2020.01.009.
[33] Ma Q, Hao B, Ma P-C. In-situ characterization on the fracture behavior of three dimensional polymer nanocomposites reinforced by CNT sponge. Composites Science and Technology 2022;217:109132. https://doi.org/10.1016/j.compscitech.2021.109132.
[34] Zhao W, Li T, Li Y, O'Brien DJ, Terrones M, Wei B, et al. Mechanical properties of nanocomposites reinforced by carbon nanotube sponges. Journal of Materiomics 2018;4:157–64. https://doi.org/10.1016/j.jmat.2018.01.006.
[35] Jiang S, Agarwal S, Greiner A. Low-Density Open Cellular Sponges as Functional Materials. Angew Chem Int Ed 2017;56:15520–38. https://doi.org/10.1002/anie.201700684.
[36] Korczeniewski E, Bryk P, Kowalczyk P, Wilczewska AZ, Boncel S, Jędrysiak R, et al. From Hansen solubility parameters to new anti-icing, viscoelastic sponges of terpolymer of tetrafluoroethylene, vinylidenefluoride, and hexafluoropropylene (THV). Chemical Engineering Journal 2024;482:148777. https://doi.org/10.1016/j.cej.2024.148777.
[37] Łapińska A, Grochowska N, Filak K, Dużyńska A, Polański M, Wyrębska I, et al. Flexible carbon-based fluoropolymer composites for effective EMI shielding and heat dissipation. Polymer Composites 2024;45:4319–37. https://doi.org/10.1002/pc.28061.
[38] Saji VS. Carbon nanostructure-based superhydrophobic surfaces and coatings. Nanotechnology Reviews 2021;10:518–71. https://doi.org/10.1515/ntrev-2021-0039.
[39] Wu C, Geng H, Tan S, Lv J, Wang H, He Z, et al. Highly efficient solar anti-icing/deicing *via* a hierarchical structured surface. Mater Horiz 2020;7:2097–104. https://doi.org/10.1039/D0MH00636J.
[40] Ijaz A, Miko A, Demirel AL. Anti-icing agent releasing diatomaceous earth/SBS composites. New J Chem 2018;42:8544–52. https://doi.org/10.1039/C8NJ01323C.
[41] Heydari G, Thormann E, Järn M, Tyrode E, Claesson PM. Hydrophobic Surfaces: Topography Effects on Wetting by Supercooled Water and Freezing Delay. J Phys Chem C 2013;117:21752–62. https://doi.org/10.1021/jp404396m.
[42] Liu X, Chen H, Zhao Z, Yan Y, Zhang D. Slippery liquid-infused porous electric heating coating for anti-icing and de-icing applications. Surface and Coatings Technology 2019;374:889–96. https://doi.org/10.1016/j.surfcoat.2019.06.077.
[43] Song M, Dang C, Higashi T, Hihara E. Review of experimental data associated with the solidification characteristics of water droplets on a cold plate surface at the early frosting stage. Energy and Buildings 2020;223:110103. https://doi.org/10.1016/j.enbuild.2020.110103.
[44] Korczeniewski E, Bryk P, Koter S, Kowalczyk P, Zięba M, Łępicka M, et al. Are nanohedgehogs thirsty? Toward new superhydrophobic and anti-icing carbon nanohorn-polymer hybrid surfaces. Chemical Engineering Journal 2022;446:137126. https://doi.org/10.1016/j.cej.2022.137126.
[45] Sprynskyy M, Pomastowski P, Hornowska M, Król A, Rafińska K, Buszewski B. Naturally organic functionalized 3D biosilica from diatom microalgae. Materials & Design 2017;132:22–9. https://doi.org/10.1016/j.matdes.2017.06.044.
[46] Nowak AP, Sprynskyy M, Brzozowska W, Lisowska-Oleksiak A. Electrochemical behavior of a composite material containing 3D-structured diatom biosilica. Algal Research 2019;41:101538. https://doi.org/10.1016/j.algal.2019.101538.
[47] Kujawa J, Al-Gharabli S, Korczeniewski E, Bryk P, Olewnik-Kruszkowska E, Kujawski W, et al. Toward effective fluorinated terpolymer-based materials for desalination with superior mechanical, chemical and anti-icing features. Desalination 2024;573:117227. https://doi.org/10.1016/j.desal.2023.117227.
[48] Malde AK, Zuo L, Breeze M, Stroet M, Poger D, Nair PC, et al. An Automated Force Field Topology Builder (ATB) and Repository: Version 1.0. J Chem Theory Comput 2011;7:4026–37. https://doi.org/10.1021/ct200196m.

[49] Stroet M, Caron B, Visscher KM, Geerke DP, Malde AK, Mark AE. Automated Topology Builder Version 3.0: Prediction of Solvation Free Enthalpies in Water and Hexane. J Chem Theory Comput 2018;14:5834–45. https://doi.org/10.1021/acs.jctc.8b00768.
[50] Molinero V, Moore EB. Water Modeled As an Intermediate Element between Carbon and Silicon. J Phys Chem B 2009;113:4008–16. https://doi.org/10.1021/jp805227c.
[51] Thompson AP, Aktulga HM, Berger R, Bolintineanu DS, Brown WM, Crozier PS, et al. LAMMPS - a flexible simulation tool for particle-based materials modeling at the atomic, meso, and continuum scales. Computer Physics Communications 2022;271:108171. https://doi.org/10.1016/j.cpc.2021.108171.
[52] Włoch J, Terzyk AP, Wiśniewski M, Kowalczyk P. Nanoscale Water Contact Angle on Polytetrafluoroethylene Surfaces Characterized by Molecular Dynamics–Atomic Force Microscopy Imaging. Langmuir 2018;34:4526–34. https://doi.org/10.1021/acs.langmuir.8b00257.
[53] Terzyk AP, Bryk P, Korczeniewski E, Kowalczyk P, Zawadzka A, Płóciennik P, et al. Water Nanodroplet on a Hydrocarbon "Carpet"—The Mechanism of Water Contact Angle Stabilization by Airborne Contaminations on Graphene, Au, and PTFE Surfaces. Langmuir 2019;35:420–7. https://doi.org/10.1021/acs.langmuir.8b03790.
[54] Meier A von. Electric power systems: a conceptual introduction. Hoboken, N.J: Wiley-Interscience [u.a.]; 2006.
[55] Tembei SAN, Hessein A, Fath El-Bab AMR, El-Moneim AA. A low voltage, flexible, graphene-based electrothermal heater for wearable electronics and localized heating applications. Materials Today: Proceedings 2020;33:1840–4. https://doi.org/10.1016/j.matpr.2020.05.182.
[56] Lupi L, Hudait A, Molinero V. Heterogeneous Nucleation of Ice on Carbon Surfaces. J Am Chem Soc 2014;136:3156–64. https://doi.org/10.1021/ja411507a.
[57] Steinhardt PJ, Nelson DR, Ronchetti M. Bond-orientational order in liquids and glasses. Phys Rev B 1983;28:784–805. https://doi.org/10.1103/PhysRevB.28.784.
[58] Pabst W, Uhlířová T, Gregorová E, Wiegmann A. Young's modulus and thermal conductivity of closed-cell, open-cell and inverse ceramic foams – model-based predictions, cross-property predictions and numerical calculations. Journal of the European Ceramic Society 2018;38:2570–8. https://doi.org/10.1016/j.jeurceramsoc.2018.01.019.
[59] Zhang L, Wang H, Xing C, Tan Y, Zhang J. Study on the influencing factors of mechanical properties of anti-icing modified asphalt mortar. Cold Regions Science and Technology 2024;223:104218. https://doi.org/10.1016/j.coldregions.2024.104218.
[60] Suppanucroa N, Nimpaiboon A, Boonchuay K, Khamkeaw A, Phisalaphong M. Green composite sponge of natural rubber reinforced with cellulose filler using alginate as a dispersing agent. Journal of Materials Research and Technology 2023;27:3119–30. https://doi.org/10.1016/j.jmrt.2023.10.139.
[61] Abdullah TA, Juzsakova T, Hafad SA, Rasheed RT, Al-Jammal N, Mallah MA, et al. Functionalized multi-walled carbon nanotubes for oil spill cleanup from water. Clean Techn Environ Policy 2022;24:519–41. https://doi.org/10.1007/s10098-021-02104-0.
[62] Li G, Quan K, Liang Y, Li T, Yuan Q, Tao L, et al. Graphene-Montmorillonite Composite Sponge for Safe and Effective Hemostasis. ACS Appl Mater Interfaces 2016;8:35071–80. https://doi.org/10.1021/acsami.6b13302.
[63] Wang L, Liu C, Huang Q, An Y, Fan J, Liu Y. A polyamide 6–organic montmorillonite composite sponge by large-scale solution foaming as a reusable and efficient oil and organic pollutant sorbent. Soft Matter 2019;15:9066–75. https://doi.org/10.1039/C9SM01444F.
[64] Park E, Ryu JH, Lee D, Lee H. Freeze–Thawing-Induced Macroporous Catechol Hydrogels with Shape Recovery and Sponge-like Properties. ACS Biomater Sci Eng 2021;7:4318–29. https://doi.org/10.1021/acsbiomaterials.0c01767.
[65] Choy CL, Luk WH, Chen FC. Thermal conductivity of highly oriented polyethylene. Polymer 1978;19:155–62. https://doi.org/10.1016/0032-3861(78)90032-0.

[66] Mu B, Li X, Feng X, Li Y, Ding C, Zhao G, et al. Relation of the Electrical Conductivity and the Thermal Conductivity to the Young's Modulus of Buckypapers. Int J Thermophys 2021;42:50. https://doi.org/10.1007/s10765-021-02806-z.
[67] Pabst W, Gregorová E. Critical Assessment 18: Elastic and thermal properties of porous materials – rigorous bounds and cross-property relations. Materials Science and Technology 2015;31:1801–8. https://doi.org/10.1080/02670836.2015.1114697.